

**Electrical Properties of Human Tissues Applied to
Wearable Antenna Design**

by

Xavier Palomer Ripoll

B.A., University of Barcelona, 2008

A thesis submitted to the
Faculty of the Graduate School of the
University of Colorado in partial fulfillment
of the requirements for the degree of
Master of Science
Department of Electrical, Computer, and Energy Engineering

2012

This thesis entitled:
Electrical Properties of Human Tissues Applied to Wearable Antenna Design
written by Xavier Palomer Ripoll
has been approved for the Department of Electrical, Computer, and Energy Engineering

Dr. Zoya Popovic

Dr. Edward Kuester

Dr. Frank Barnes

Date _____

The final copy of this thesis has been examined by the signatories, and we find that both the content and the form meet acceptable presentation standards of scholarly work in the above mentioned discipline.

Palomer Ripoll, Xavier (M.C., Electrical Engineering)

Electrical Properties of Human Tissues Applied to Wearable Antenna Design

Thesis directed by Dr. Zoya Popovic

A method for designing wearable antennas at microwave frequencies is presented in this thesis. An antenna placed on the human body is heavily influenced by the electrical properties of tissues. Thus, the proposed method includes the development of mixtures that mimic the electrical properties of human tissues in order to validate the antenna designs. Simulation of several printed antennas in the presence of tissues are performed and analyzed.

The work outlines the process of developing phantom tissues and their validation using an open-ended coaxial probe method. A guide-wave permittivity measurement method and a free space measurement method are also discussed. The results show lower values than expected for the complex permittivity compared to those previously published. Some reasons for the discrepancy are suggested.

Two prototype antennas are developed: a rectangular patch antenna and a dipole. A layered stack model of tissues is compared to a simpler and computationally more efficient half space model. The effect of the separation between the antenna and the tissues, the bending of tissues and the variation of tissue electrical characteristics is analyzed and quantified. The separation or bending of the tissues greatly influences the performance of the antenna, as expected.

Dedication

A l'avi Josep...

Espero que on estiguis aquesta tesis et fagi sentir orgullós i feliç. Del teu nét amb carinyo...

Acknowledgements

This work was made possible by the Balsells fellowship from the Balsells Foundation, the University of Colorado and the Generalitat de Catalunya. Special thanks to Pete Balsells and Rob Davis for supporting the Balsells program at the University of Colorado at Boulder and to everyone that made this fellowship possible.

I thank Zoya Popovic for being my graduate advisor and for encouraging and reinforcing me during this period. Without her help this work would not be possible.

I want to thank the students from the Microwave Active Antenna and Circuits group that have deeply enriched my personal experiences and scientific knowledge. I want to specially thank Rob Shceeler and Frank Trang for their help on this learning process, Jose Angel Garcia for his support and Ved Topkar for his helpful collaboration.

My family and friends were an incredible support during this period. Although they were far away in distance, my family is being a great support and I always felt their warmth. I want to thank my parents Marta and Xavier and my grandparents Roser, Berta and Carles for their support all my life and for teaching me everything I know. I want to thank my brothers Carles and Ferran for sharing their experiences with me. I want to thank Laura Bernabe, Eric Antillon and Ignacio Ramos for their support these two years far away from home. I want to thank Maria Quiñones for her support. I want to thank all my friends from Girona, thanks Kalaiaia.

Finally, and as a special remark, I want to thank Pete Balsells and my grandfather for their encouraging support during this period. Without them I would have never achieved this personal challenge.

Contents

Chapter	
1	Introduction 1
1.1	Electrical properties of biological and phantom tissues 5
1.1.1	Overview of dielectric properties 6
1.1.2	Biological tissue properties 11
1.1.3	Phantom tissues 13
1.2	Wearable antenna 15
2	Phantom tissues 19
2.1	Phantom tissues mixing process 20
2.1.1	Procedure for making phantom skin tissues 20
2.1.2	Procedure for making phantom muscle tissues 21
2.1.3	Procedure for making phantom fat tissues 21
2.2	Phantom tissue validation 22
2.2.1	Free space measurements 23
2.2.2	Microstrip based measurements 26
2.2.3	Open-ended coaxial probe 30
3	Wearable antenna 49
3.1	Dipole antenna on tissue 53
3.1.1	Antenna design and performance 54

3.2	Patch antenna on tissue	58
3.2.1	Antenna design	59
3.2.2	Antenna performance	59
3.3	Effects of tissue antenna separation and tissue bending	60
3.3.1	Effects on the dipole	62
3.3.2	Effects on the patch antenna	66
3.4	Tissue variation effects on antenna performance	68
4	Conclusions and future work	74
4.1	Summary	75
4.2	Future work	76
4.3	Conclusions	77

List of Tables

Table

2.1	Reference materials used to extract C_s and C_t parameters.	42
-----	---	----

List of Figures

Figure

1.1	Examples of antennas used in biological applications. Figure 1.1(a) shows a hyperthermia device placed on a chest of a woman to perform hyperthermia cancer treatment, [1]. Figure 1.1(b) shows antennas for breast cancer detection published in [2]. Figure 1.1(c) shows wearable or implanted antennas used to create a Local Area Network (LAN) to communicate between hospitals, doctors or health care centers for patient monitoring [3]. Figure 1.1(d) shows implantable device geometry used to study packaging and performance in the near-field [4].	2
1.2	Block diagram of a Dicke radiometer. The input signal to the Low Noise Amplifier (LNA) is switched between the desired signal received by the antenna and a known noise power source which is used for online calibration.	5
1.3	Comparison between Debye (solid blue line) and Cole-Cole (dashed red line) models. Normalized permittivity $(\epsilon' - \epsilon_\infty) / (\epsilon_s - \epsilon_\infty)$ and loss factor $\epsilon'' / (\epsilon_s - \epsilon_\infty)$ are plotted against the resonant frequency, showing a typical resonance defined by the models previously stated.	10
1.4	Dependence of permittivity (Figure 1.4(a)) and conductivity of water (Figure 1.4(b)) with temperature. Only one resonance is taken into account for these plots because of the frequency range of interest. Temperature dependence taken from [5].	11

1.5 Typical frequency dependence of material with complex permittivity such as biological tissues where the three typical relaxation processes (α , β and γ) are shown. The behavior of a typical human tissue follows the plot shown in this figure. In some cases some other relaxation processes could appear (e.g. δ). The plot is taken from [6]. 13

1.6 Permittivity (on the left) and conductivity (on the right) variations in skin and their effects on antenna performance are shown. The configuration used in these plots is a patch antenna in contact with the stack of tissues presented in Figure 3.1(b). From these two figures the required accuracy is $\epsilon_r = \pm 1$ and $\sigma = \pm 0.1$ S/m. Thus, phantom tissues measurements require this precision. 15

1.7 Example of wearable antenna used in military applications, Figure 1.7(a), taken from [7], represents a printed antenna on a person's skin; Figure 1.7(b), taken from [8], shows an antenna integrated on fabric for communications purposes; and Figure 1.7(c), taken from [9], shows different antennas that a soldier might carry in the future on a standard uniform. 17

1.8 Comparison of the radiation patter of a PIFA antenna designed to be used on a handset for the two GSM bands with and without the presence of the user. On the left the radiation patter of the antenna in free space. On the left the modified radiation pattern in the presence of head and hand. Frequencies are 1 and 2GHz, the antenna is a PIFA antenna used in a Sony-Ericsson handset. Red means high power and green low power. Pictures are taken from [10]. . . 18

2.1 Photo of skin (green) and muscle (red) final mixtures 22

2.2 Free space measurement setup, with phantom muscle tissue between the two antennas connected to the VNA. As shown, the two antennas are the two ports used. The two antennas must be at least at the far field distance from the tissues. 24

2.3	Free space measurements technique equivalent transmission model. The ports represent the two antennas shown in Figure 2.2.	25
2.4	Cross section of the microstrip fixture with the lossy material on top.	27
2.5	Flowchart of method used to extract superstrate electrical properties	27
2.6	Simulations performed for the Thru microstrip standard. 2.6(a) with sigma 1s/m epsilon relative varied between 5-60 and the resulting amplitude of S_{11} is shown. 2.6(b) with epsilon 10 sigma varied between 5-60 and the resulting amplitude of S_{11} is shown.	28
2.7	Simulations performed for the Reflect microstrip standard. 2.7(a) with sigma 1S/m epsilon relative varied between 5-60 and the resulting amplitude of S_{11} is shown. 2.7(b) with epsilon 10 sigma varied between 0.5-1.6S/m and the resulting amplitude of S_{11} is shown.	28
2.8	Simulations performed for the Thru microstrip standard. 2.8(a) with sigma 1s/m epsilon relative varied between 5-60 and the resulting amplitude of S_{21} is shown. 2.8(b) with epsilon 10 sigma varied between 5-60 and the resulting amplitude of S_{21} is shown.	29
2.9	Open-ended coaxial probe used at the National Institute for Standards and Technology. The probe has different dimensions depending of the frequency range of interest. Figure 2.9(a) shows the probe. Figure 2.9(b) shows the probe with the MUT on top. In our case the tissue material was not firm, so it was placed under the probe. Courtesy: Dr. Michael Janezic, NIST Boulder	31
2.10	Equivalent circuit of the open-ended coaxial probe, where the material is modeled as a capacitor and a resistor in parallel denoting the real and imaginary part of the permittivity	33
2.11	Open-ended coaxial probe used to measure liquid dielectric properties. The system has a thermostat bath that allows temperature measurements. The sketch shows the system for blood measurements and is taken from [11].	36

2.12	Coordinate system used. Subscripts 0, 1 and 2 denote air, dielectric inside the coaxial line and dielectric outside the coaxial line, respectively	39
2.13	Results of simulations for material ($\epsilon = 2.05$) with material used in the literature ([12, 13, 14]) and extracted from [15]. In the simulation the cable connecting the probe and the source has some length but in the previously mentioned publication [16] it has no length. A small shift to lower values is observed, mainly because of the length of the coaxial probe.	40
2.14	C_s extraction curve from reference materials listed in [16]. Solid line is least-squares fit of the sample capacitance measured for known materials (blue cross).	41
2.15	Dielectric constant of reference material ($\epsilon_r = 2.05$) used to extract required parameters C_s and C_t and to validate simulations.	43
2.16	Results of simulations for skin (top) and muscle (bottom). The permittivity is plotted in blue and the conductivity is plotted in red. Solid lines are from Gabriel's publication and dashed lines are results from simulations.	44
2.17	Results of measuring skin at NIST with Michael Janezic. Results are discussed on section 2.2.3.3	45
2.18	Results of measuring muscle phantom tissue at NIST with Michael Janezic. Results are discussed in section 2.2.3.3. Measurements are lower than expected.	46
2.19	Contact between the probe and the sample surface. As the MUT is rough, the contact between the probe and the MUT might not be perfect, leading to an air gap. This air gap could be modeled as a capacitance which will decrease the values measured. Picture taken from [14].	48

3.1	Models used along with the antennas in order to study their performance in contact with dielectrics. On top the half space tissue model, where the antenna is placed on the top of the phantom. On the bottom, the layered model mimicking the human chest.	52
3.2	Sketch of dipole antenna used on simulations. Particularly, the antenna shown here, has a resonant frequency at 1.41GHz and a length of $l = 14.5mm$. . .	54
3.3	Optimization of dipole length on top of the stack of tissues shown in Figure 3.1(b). The left plot shows the relation between length and frequency. In red is the length of the dipole in contact with tissues and in blue the same length radiating on free space. In the right plot the effective dielectric constant was calculated from the previous relation.	56
3.4	Comparison of the resonant frequency between the antenna on top of the stack of tissues and radiating into free space. Figure 3.4(a) shows in red the S_{11} magnitude in dB of the dipole response radiating in contact with tissues; the same figure but in blue shows the S_{11} magnitude in dB of the antenna performing without the tissues, i.e. radiating into free space. Figure 3.4(b) shows the real (solid lines) and imaginary (dashed lines) parts of the input impedance of the antenna with (in red) and without the tissues (in blue). Figure 3.4(a) is normalized to a 50Ω characteristic impedance line.	57
3.5	Drawing of the antenna design in free-space. It is important to note the ground plane shape being narrower in the radiation side of the antenna (L side).	60
3.6	Comparison of the antenna's performance in free space and in contact with tissues, in blue and red respectively in both figures. Figure 3.6(a) plots the magnitude of the S_{11} parameter. Figure 3.6(b) shows imaginary (dashed lines) and real (solid lines) parts of the input impedance. Figure 3.6(a) is normalized to a 50Ω characteristic impedance line.	61

- 3.7 Sketch of the different scenarios studied with the dipole antenna. 3.7(a) shows the dipole on top of the stack of tissues; 3.7(b) shows the dipole on top of the stack of tissues having a perpendicular separation between the tissues and the antenna; 3.7(c) shows the dipole on top of the stack of tissues with one side separation; and 3.7(d) shows the dipole on top of the stack of tissues with both sides separation. 63
- 3.8 Sketch of the different scenarios studied with the patch antenna. 3.8(a) shows the patch on top of the stack of tissues; 3.8(b) shows the patch on top of the stack of tissues having perpendicular separation between the tissues and the antenna; 3.8(c) shows the patch on top of the stack of tissues with one side separation; and 3.8(d) shows the patch on top of the stack of tissues with both sides separation. 64
- 3.9 Frequency of operation of the dipole performing in the different scenarios described before in Figure 3.7. Figure 3.9(a) shows the optimum frequency of operation. Figure 3.9(b) shows the magnitude of the reflection coefficient at the operating frequency (1.41GHz). The figures show in red the effects of one side bending , in green the effects of two sides bending and in blue the perpendicular separation effects. 65
- 3.10 The plot shows how the bending of the tissues affect the input impedance of the dipole. Figure 3.10(a) plots the input resistance and Figure 3.10(b) shows the input reactance. The figures show in red the effects of one side bending , in green the effects of two sides bending and in blue the perpendicular separation effects. 66

3.11 Performance of the patch in the different scenarios described before. Figure 3.11(a) shows the optimum frequency of operation. Figure 3.11(b) shows the magnitude of the reflection coefficient at the operating frequency. Figures show in blue the perpendicular separation between the antenna and the dipole; in green the one edge bending, being L side dark green and W side light green; in purple the two edge bending along W side and in red the two edges bending along L side. 67

3.12 These plots show how the bending of the tissues affect the input impedance of the patch. Figure 3.12(a) shows the input resistance and Figure 3.12(b) shows the input reactance of the patch antenna. Figures show in blue the perpendicular separation between the antenna and the dipole; in green the one edge bending, being L side dark green and W side light green; in purple the both edges bending along W side and in red both edges bending along L side. 68

3.13 The figure shows the optimum length of the dipole in contact with the different tissues. The model used is the half space phantom, shown in Figure 3.1(a). 69

3.14 Figure 3.14(a) shows the variation of the optimum frequency of operation of the dipole due to variations in the dielectric constant of the tissues. Figure 3.14(b) shows the variation the magnitude of the reflection coefficient of the dipole at the designed frequency (1.41GHz) due to tissue dielectric constant variations. Figures show the conductivity variation of the skin in blue, of the fat in green, of the first layer of cortical bone in red, of the cancellous bone in cyan, of the second layer of cortical bone in magenta and of the muscle in yellow. 70

- 3.15 Figure 3.15(a) shows the variation of the input resistance of the dipole at the designed frequency (1.41GHz) due to variations in the dielectric constant of the tissues. Figure 3.15(b) shows the variation of input reactance of the dipole at the designed frequency (1.41GHz) due to variations in the dielectric constant of the tissues. Figures show the conductivity variation of the skin in blue, of the fat in green, of the first layer of cortical bone in red, of the cancellous bone in cyan, of the second layer of cortical bone in magenta and of the muscle in yellow. 71
- 3.16 Figure 3.16(a) shows the variation of the optimum frequency of operation of the dipole due to variations in the conductivity of the tissues. Figure 3.16(b) shows the variation of the reflection coefficient magnitude of the dipole at the designed frequency (1.41GHz) due to variations in the conductivity of the tissues. Figures show the conductivity variation of the skin in blue, of the fat in green, of the first layer of cortical bone in red, of the cancellous bone in cyan, of the second layer of cortical bone in magenta and of the muscle in yellow. 72
- 3.17 Figure 3.17(a) shows the variation of input resistance of the dipole at the designed frequency (1.41GHz) due to tissue variations in the conductivity of the tissues. Figure 3.17(b) shows the variation of input reactance of the dipole at the designed frequency (1.41GHz) due to tissue conductivity variation. Figures show the conductivity variation of the skin in blue, of the fat in green, of the first layer of cortical bone in red, of the cancellous bone in cyan, of the second layer of cortical bone in magenta and of the muscle in yellow. 73

Chapter 1

Introduction

Contents

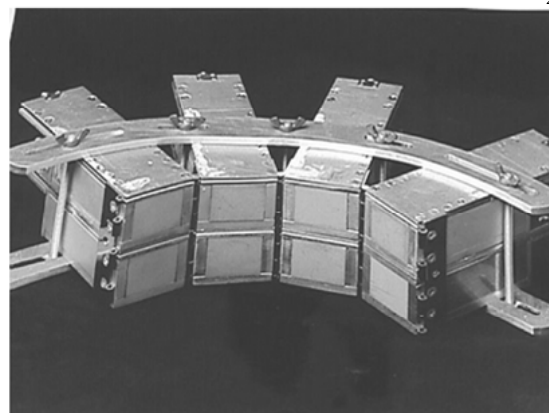
1.1	Electrical properties of biological and phantom tissues	5
1.1.1	Overview of dielectric properties	6
1.1.2	Biological tissue properties	11
1.1.3	Phantom tissues	13
1.2	Wearable antenna	15

In the last few decades, microwave techniques in biological applications have been a topic of increased research and development [17, 18]. Most of these applications include some type of radiating structure, examples include:

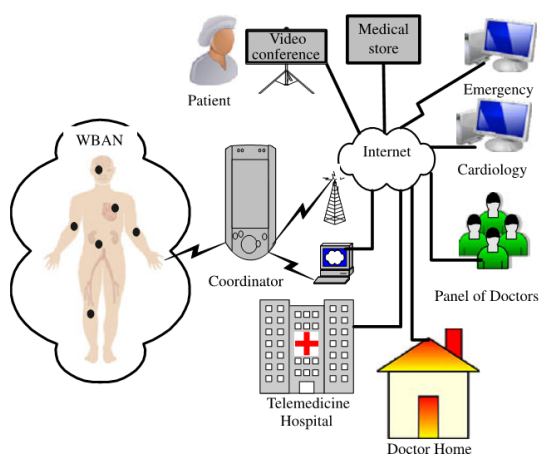
- (1) various types of antennas have been used for hyperthermia treatment of cancer, heating tumors up to 44°C for more than 30 min, Figure 1.1(a) [1];
- (2) antennas have been used to detect breast cancer with a probability of detection of around 80%, Figure 1.1(b). Different systems have been used on these studies, e.g., Rank Thermographic System [19], with a good comparison reported in [20];



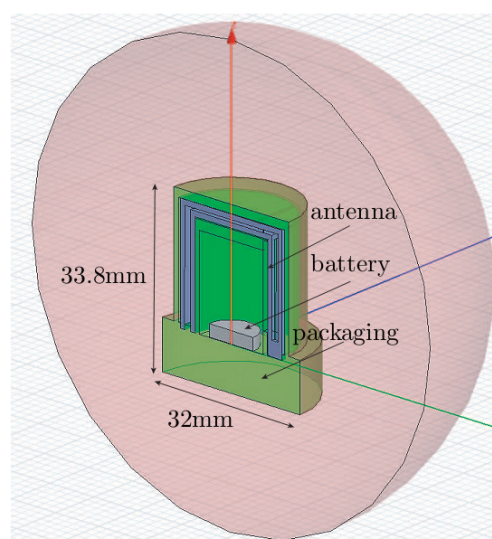
(a)



(b)



(c)



(d)

Figure 1.1: Examples of antennas used in biological applications. Figure 1.1(a) shows a hyperthermia device placed on a chest of a woman to perform hyperthermia cancer treatment, [1]. Figure 1.1(b) shows antennas for breast cancer detection published in [2]. Figure 1.1(c) shows wearable or implanted antennas used to create a Local Area Network (LAN) to communicate between hospitals, doctors or health care centers for patient monitoring [3]. Figure 1.1(d) shows implantable device geometry used to study packaging and performance in the near-field [4].

- (3) wireless body area network where wearable antennas are used for communication between miniaturized body sensors (BSU) in a single network, Figure 1.1(c) [3];
- (4) in 2005, RF System Lab announced its next generation endoscopic wireless capsule which uses RF inductive powering instead of a battery and is capable of transmitting 870,000 images during its 8 hours lifecycle, Figure 1.1(d) [4];
- (5) Microwave radiometers with antennas placed against skin of a patient have been used for thermometry of the human body, described in more detail below [21, 22, 23].

Sketches of these examples are shown in Figure 1.1. The antennas are placed close to or implanted in the body, so it is extremely important to understand the performance of antennas in contact with human tissues in order to develop accurate models for all the applications listed above. The challenge of modeling an antenna in proximity of human tissue comes from complex and frequency dependent electrical properties of various tissues and variation throughout different body types.

The antenna characterization in the presence of tissues presented in this thesis is focused on the microwave thermometry application. Here, an antenna placed in the near field of a body is used to detect noise power radiated from different tissues inside the body. Internal body temperature measurements are important in several applications, such as: (1) medical diagnostics, e.g., monitoring deep brain temperature of newborn infants [21]; (2) detecting tumors [20]; (3) studying the circadian cycle [24]; (4) monitoring people under physical stress, e.g., military personnel and athletes; and (5) monitoring emergency workers under extreme conditions.

Currently, there are no commercial technologies for internal body temperature measurements. Internal body temperature can be estimated from several external measurements, but these methods are not reliable. Another approach used in the military for monitoring overheating of soldiers under heavy training or in hot climates is a wireless pill thermometer which remains in the body an unknown length of time and only measures temperature of

the intestine [25]. Furthermore, there are different methods, which can be very invasive and extremely uncomfortable for patients, such as rectal temperature measurements, using a normal mercury thermometer or a special probe; and esophageal temperature measurements, using a thermistor inserted through the nasal passages which can cause irritation. A common method is the use of infrared (IR) thermometers, which only measures surface temperature and are usually tympanic, i.e. inserted in the ear [26].

Microwave thermometry consists of measuring black body radiation from an object and extracting temperature from power measurements using a microwave radiometer. A specific Dicke radiometer is shown in Figure 1.2 [27], where the antenna is usually in the far-field of the object under test, such as in a radio telescope. In this work, a study of the feasibility of wearable antennas for radiometric measurements in the near field is presented. Full wave electromagnetic simulation software HFSS (High Frequency Structure Simulation), based on FEM (Finite Element Method); and SEMCAD-X, based on FDTD (Finite Difference Time Domain) are used to simulate the effects of radiation from tissues on the antenna and, subsequently, for antenna design. In order to enable realistic measurements that do not involve live samples, phantom tissues are developed and their electric properties are measured and used as validation of the simulations.

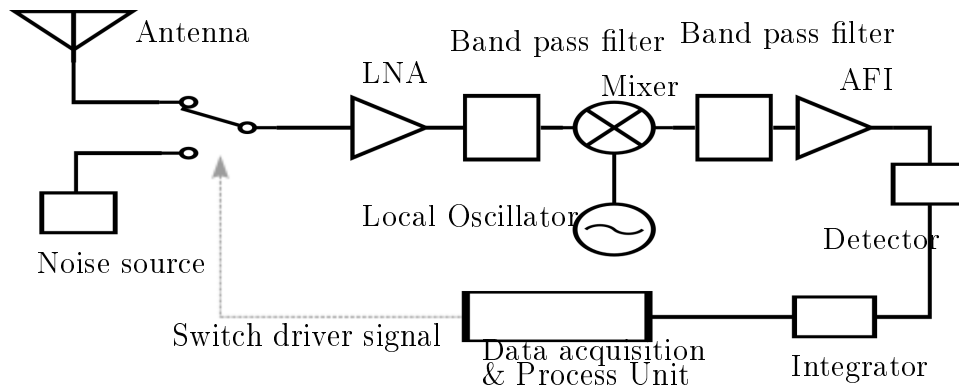


Figure 1.2: Block diagram of a Dicke radiometer. The input signal to the Low Noise Amplifier (LNA) is switched between the desired signal received by the antenna and a known noise power source which is used for online calibration.

1.1 Electrical properties of biological and phantom tissues

Knowledge of dielectric properties of tissues is important background in studying the effects of electromagnetic (EM) fields on biological systems. Current research investigates the theoretical aspects of the interaction between living matter and EM fields. In most cases, the interaction is described qualitatively and only some threshold limits are placed in order to avoid human exposure to radio frequency radiation. It is commonly accepted to treat tissues as homogeneous materials with some defined electrical characteristics. In reality, tissues are inhomogeneous materials, with different levels of complexity. One can take a look into living tissues and find different types of cells (muscle cells, neurons,...) arranged in different structures, depending what type of tissue is studied. Moreover, between cells, different tissues have different extracellular fluid. These inhomogeneities result in a system that is difficult to model. The relevant scale is related to the EM wave frequency; at higher frequencies corresponding to smaller wavelengths, more complexity of the tissue should be taken into account. In this work, the wavelength of EM radiation in air is on the order of 10 to 50cm so that average values for tissue parameters can be used.

Electric and magnetic properties are defined by conductivity (σ), permittivity (ϵ) and

permeability (μ), from the constitutive relations of Maxwell's equations for linear media given as:

$$\vec{D} = \epsilon_0 \vec{E} + \vec{P} = \epsilon_0 \epsilon_r \vec{E} = \epsilon(x, y, z) \vec{E} \quad (1.1)$$

$$\vec{B} = \mu_0 (\vec{H} + \vec{M}) = \mu_0 \mu_r \vec{H} = \mu \vec{H} \quad (1.2)$$

where \vec{E} is the electric field vector, \vec{H} is the magnetic vector, \vec{J} is the current density vector, \vec{D} is the displacement vector, \vec{P} is the dielectric polarization vector, \vec{B} is the magnetic flux density vector and \vec{M} is the magnetization vector. ϵ_0 and μ_0 are fundamental constants, $\epsilon_0 \approx 8.8541878... \times 10^{-12}$ F/m and $\mu_0 = 4\pi \times 10^{-7}$ H/m.

Tissues are dispersive materials, and different models are applied to describe permittivity as a function of frequency. Most commonly accepted is the Cole-Cole model for dielectric materials with relaxation processes. A special case of the Cole-Cole model is the Debye model, which is also widely accepted. The most relevant articles for living tissues measurements include: Gabriel 1996 [28], Schawn 1994[29] and Athey 1982 [30]. Data agrees with theoretical models and presents different relaxation processes that lead to different relaxation times. The most commonly used measurement method is an open-ended coaxial probe placed in contact with the desired tissue. This method is only applicable to *in vitro* tissues and is not applicable to *in vivo* measurements.

1.1.1 Overview of dielectric properties

Permittivity is the intrinsic characteristic of matter that determines the matter-electric field interaction. Permittivity values of living matter vary significantly, from high values (close to water, $\epsilon_r \sim 80$) to low values (close to vacuum, $\epsilon_r = 1$).

The permittivity for linear materials given in equation 1.5 can be expressed as a complex number for lossy materials in time-harmonic fields. Working using phasors, assuming

fields are of the form $\cos(\omega t)$ and assuming the material with conductivity:

$$\vec{J} = \sigma \vec{E} \quad (1.3)$$

Maxwell's curl equation for \vec{H} becomes:

$$\begin{aligned} \nabla \times \vec{H} &= j\omega \vec{D} + \vec{J} \\ &= j\omega \epsilon \vec{E} + \sigma \vec{E} \\ &= j\omega \left(\epsilon' - j \frac{\sigma}{\omega} \right) \vec{E} \end{aligned} \quad (1.4)$$

assuming conductive losses (ohmic) are much larger than polarization losses. From the previous equation we define a complex permittivity as:

$$\hat{\epsilon} = \epsilon_0 \epsilon_r - j \frac{\sigma}{\omega} = \epsilon' - j\epsilon'' \quad (1.5)$$

and a related quantity is the loss tangent defined as:

$$\tan \delta = \frac{\sigma}{\omega \epsilon'} \quad (1.6)$$

where ϵ' is the real part of the permittivity and describes the capability of the medium to become polarized and store energy. The real part of the permittivity is characterized by the dielectric constant ϵ_r , where $\epsilon' = \epsilon_0 \epsilon_r$. The imaginary part ϵ'' is related to losses in the medium due to conduction described by conductivity σ from Ohm's law, Equation 1.3. ϵ'' thus gives a measure of dissipated (absorbed) power.

The field matter interaction does not happen instantaneously, resulting in a frequency dependance of the complex permittivity. This dispersion effect is often characterized by a relaxation time analogous to an RC constant in an electrical circuit. By combining Gauss' law and the continuity equation for time-varying charges, the relaxation time can be obtained as follows:

$$\nabla \cdot \vec{E} = \frac{\rho}{\epsilon}$$

$$\nabla \cdot \vec{J} = -\frac{\partial \rho}{\partial t} \Rightarrow \nabla \cdot \vec{E} = -\frac{1}{\sigma} \frac{\partial \rho}{\partial t}$$

$$\frac{\rho}{\epsilon} = -\frac{1}{\sigma} \frac{\partial \rho}{\partial t} \Rightarrow \frac{\partial \rho}{\partial t} + \frac{\sigma}{\epsilon} \rho = 0 \quad (1.7)$$

The solutions to the previous differential equations are given by:

$$\rho = \rho_0 e^{-t/\tau} \quad \text{and} \quad \tau = \frac{\epsilon}{\sigma} \quad (1.8)$$

where the time constant τ is related to a capacitive term (ϵ) and to a resistance term ($1/\sigma$) and is thus analogous to the RC time constant of an electrical circuit.

At this point, is interesting to note how the material can follow electric field oscillation. If the electric field frequency is higher than the inverse of the relaxation time, the material may not follow the field and the polarization of the material is transparent to the electric field, meaning that the electric field does not affect the material. Typically, materials are defined by three relaxation times: orientational, where dipoles moment of molecules are oriented in different ways; ionic, due to atomic dipole polarization; and electronic, due to electron polarization in atoms.

1.1.1.1 Models of permittivity

There are several models to fit measured permittivity performance over frequency. The most accepted models are the Debye and the Cole-Cole models, especially for biological tissues. The Debye model is theoretically derived while the Cole-Cole model and its variation the Davidson-Cole model are derived from experimental measurements. The most most general case is the Havriliak–Negami is given by 1.9:

$$\hat{\epsilon} = \epsilon_{\infty} + \frac{\epsilon_S - \epsilon_{\infty}}{(1 + (i\omega\tau)^{\alpha})^{\beta}} \quad (1.9)$$

while the Davison-Cole is expressed by 1.10:

$$\hat{\epsilon} = \epsilon_{\infty} + \frac{\epsilon_S - \epsilon_{\infty}}{(1 + i\omega\tau)^{\beta}} \quad (1.10)$$

The Debye model is defined by the following equation:

$$\hat{\epsilon} = \epsilon_{\infty} + \frac{\epsilon_S - \epsilon_{\infty}}{1 + i\omega\tau} \quad (1.11)$$

where ϵ_s is the static value of the permittivity at $\omega \sim 0$; and ϵ_{∞} is the relative permittivity at high frequencies where contribution due to orientation disappears and electronic and ionic contributions are constant. This is a theoretical model, and in practice there are not many materials than follow this model. Figure 1.3 plots typical material characteristics as derived from the Debye model compared to the Cole-Cole model. The Cole-Cole model is an experimental model proposed in 1941 [31] and [32], and is more general than the Debye model. The equation below defines the model, where $0 \leq \alpha \leq 1$ and determines the distribution of the function:

$$\hat{\epsilon} = \epsilon_{\infty} + \frac{\epsilon_S - \epsilon_{\infty}}{1 + (i\omega\tau)^{1-\alpha}} \quad (1.12)$$

Finally, it is important to note that for a material with more than one relaxation time, in all models the result is a linear combination of one equation for each relaxation time. For example, in the case of Debye model, the resultant equation will be:

$$\hat{\epsilon} = \epsilon_{\infty} + \frac{\epsilon_S - \epsilon_{\infty}}{1 + i\omega\tau_1} + \frac{\epsilon_S - \epsilon_{\infty}}{1 + i\omega\tau_2} + \dots \quad (1.13)$$

From this brief overview it is obvious that biological materials can have complicated electrical dispersion properties which need to be taken into account when designing antennas for biological applications.

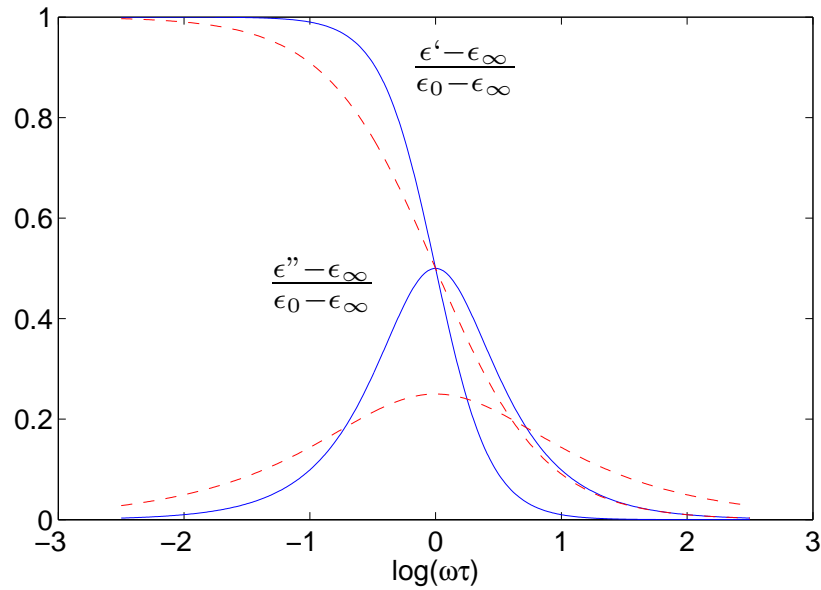


Figure 1.3: Comparison between Debye (solid blue line) and Cole-Cole (dashed red line) models. Normalized permittivity $(\epsilon' - \epsilon_\infty) / (\epsilon_s - \epsilon_\infty)$ and loss factor $\epsilon'' / (\epsilon_s - \epsilon_\infty)$ are plotted against the resonant frequency, showing a typical resonance defined by the models previously stated.

1.1.1.2 Temperature dependence

Permittivity is frequency dependent but may also be characterized by temperature dependence. The relationship between permittivity and temperature is not defined by any model, as each material has its own temperature variation. The temperature characteristics of a material are defined by measurements. It is particularly interesting to see what happens to water dielectric properties as temperature changes because human tissues consist primarily of water (the water content of the body is between 60% and 75%, [33, 34, 35]).

Pure water behaves according to the Debye model given by the Equation 1.11, ϵ_∞ , ϵ_S and τ being the three constants that define the equation. These three constants, as published in [5], decrease when temperature increases. This behavior does not lead to a perfect interpretation of dielectric constant and conductivity. Coefficients (ϵ_∞ , ϵ_S and τ)

have a variation of 1-2% over a temperature variation of 60^oC, [5, 36]. Complex permittivity temperature dependence is shown in Figure 1.4.

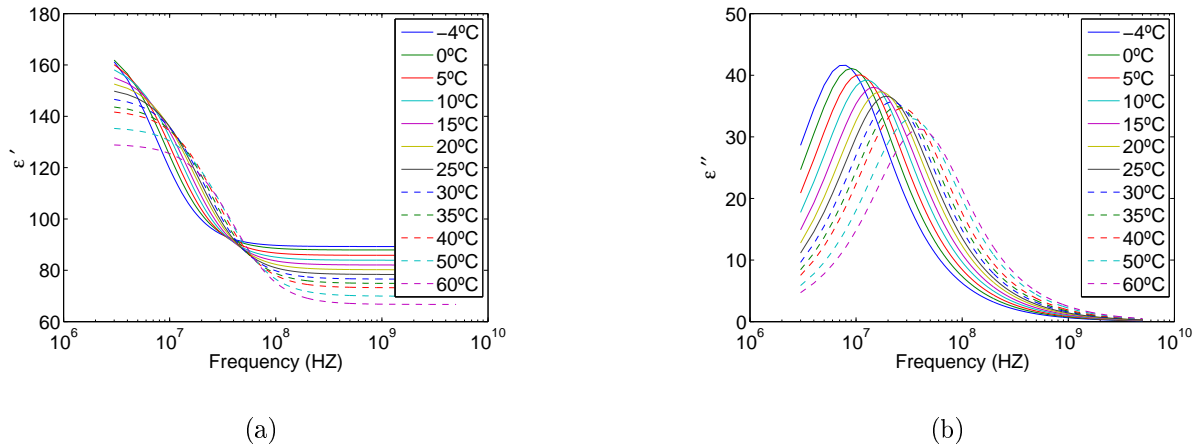


Figure 1.4: Dependence of permittivity (Figure 1.4(a)) and conductivity of water (Figure 1.4(b)) with temperature. Only one resonance is taken into account for these plots because of the frequency range of interest. Temperature dependence taken from [5].

1.1.2 Biological tissue properties

Electrical properties of biological tissues have been extensively studied on the literature. There are different publications that determine electrical properties of tissue, e.g. example Smye '07 [37], Athey '82 [30] or Schwan '94 [29]; but the most accepted standards for tissue properties are the publications from Camelia Gabriel '96 [28, 38, 39]. Gabriel's measurements are taken using open-ended coaxial probes. This technique is studied in chapter 2 section 2.2. The techniques consists of a coaxial cable with a special radiating end that interacts with the Material Under Test (MUT). This interaction between the references or the MUT and the probe leads to different reflection coefficients which are used to extract the electrical properties of the MUT. Moreover, Gabriel's measurements are carried out using dead tissues, because most of the tissues are internal to the body are impossible to measure using this technique. The procedures used in Gabriel's publications are not very well defined, as it is

difficult to define in what conditions the dead tissues are. However, temperature is given and to best simulate living tissues, tissues are used immediately after cadaver autopsy.

The data presented in all citations previously mentioned are the closest possible to living tissues taken in *in vitro* conditions for most of the results. *In vivo* measurements are carried out also for those tissues accessible with the open-ended coaxial probe. As *in vitro* measurements are difficult to validate against live tissues, the closest solution to live tissues is used. Thus, the closest temperature to body temperature and the nearest time after death are taken when possible. Human tissues are often compared with animal tissues or to live tissues in order to validate measurements.

Data is presented in graphical form, rather than tabular, and in logarithmic scale rather than linear form, because of the range of frequencies measured. Characteristics measured are dielectric constant and conductivity (rather than loss tangent or imaginary part of permittivity).

On the other hand, the temperature is important when measuring complex permittivity as explained before. As there is no model that determines this dependence only the temperature of given measurements is shown, but no model is used to explain the relation.

However, dielectric constant and conductivity for *in vivo* tissues are not standardized; there are few measurements of *in vivo* tissues for specific applications, e. g. Dieter '03 [40]. To the best of our knowledge, there are no techniques capable of measuring *in vivo* tissue properties. The only tissues measured *in vivo* are skin and tongue because they are easily accessible and measurements are not dangerous for the patient.

Human tissues relative permittivity ϵ_r ranges from around 5 for fat or narrow bone to almost 70 for cerebrospinal fluid or vitreous humor at 1 GHz. The conductivity σ ranges from 0.5 S/m for fat to 1.6 S/m for blood.

Biological tissues typically show three relaxations, related to the structure of the tissues. At low frequencies, one may observe first relaxation process, related to the ionic polarization along the cell membrane. This first relaxation process is called α dispersion or low frequency

dispersion. At higher frequencies, one can observe another relaxation process, called the β relaxation process, related to the capacitive charging of the cell membrane. And finally, at very high frequencies, there is another relaxation process called the γ relaxation process. γ dispersion is related to the dipolar polarizations of tissue water content.

These are the three more important dispersions one may find, but some materials, and of course biological materials, may have another relaxation process between those explained before. In particular, sometimes a relaxation process between β and γ processes may be observed, this dispersion is called δ dispersion. A δ process may occur due to relaxations of proteins dispersed throughout the material, as illustrated in Figure 1.5.

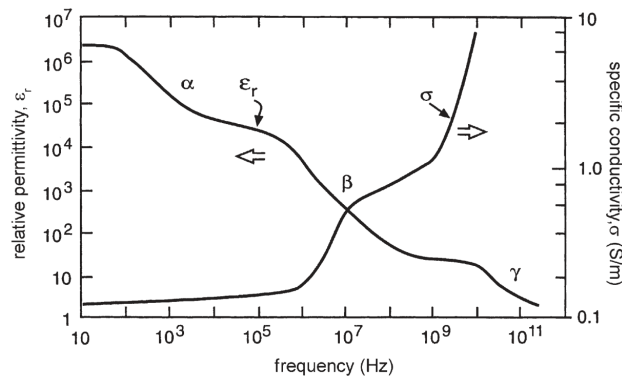


Figure 1.5: Typical frequency dependence of material with complex permittivity such as biological tissues where the three typical relaxation processes (α , β and γ) are shown. The behavior of a typical human tissue follows the plot shown in this figure. In some cases some other relaxation processes could appear (e.g. δ). The plot is taken from [6].

1.1.3 Phantom tissues

Living tissues are difficult to obtain (especially human tissues) and there are a lot of problems associated with possible measurements, e.g. dead tissues, temperature variations, etc. Instead of using living matter, one may use mixtures that mimic real tissue properties. In this document, we are interested in the electrical characteristics of tissues. Phantom

tissues can be used to mimic human tissues. These phantom tissues are mainly mixtures of water, vegetable oil (used as fat content in tissues), salt and some chemicals that can reproduce electrical properties of living tissues.

In the literature, e.g. Topsakal '08 [41] and others [42, 43, 44, 45, 46], complex methods for mixing substances are described, using expensive processes and equipment. One of the goals of this document is to develop an inexpensive method suitable to be used in any RF lab. After the mixing process is finished, validation of properties of the final mixtures should be done. In this thesis the process of creating muscle, skin and fat phantoms is presented in chapter 2.

1.1.3.1 Phantom tissues validation

In order to validate the mixtures, complex permittivity has to be measured. There are different methods to measure complex permittivity. The method we should use has to be: (1) cheap and easy to reproduce; (2) easy to implement in a standard radio frequency lab; and (3) such that it does not require high precision measurements and components, precision required is ± 1 for permittivity and ± 0.1 S/m for conductivity measurements, as shown in Figure 1.6. To obtain this plot, a patch antenna was simulated on the tissue stack shown in Figure 3.1(b) and the values of σ and ϵ were varied until a $< 2\%$ variation on the reflection coefficient magnitude was observed. From that point, we divided the variation by two and that is the final accuracy we would like to measure on the phantom tissues.

Taking into account these requirements, two methods were chosen: Open-ended coaxial cable and Free space measurements. Another method is proposed and used: TRL fixture permittivity measurements. This is a novel method fully developed and this thesis. All these methods are explained in detail in chapter 2 section 2.2.

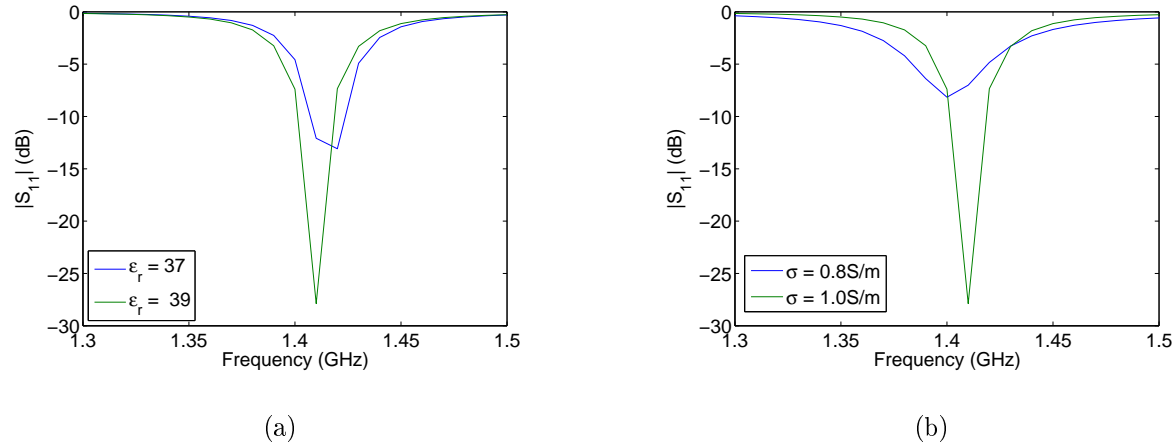


Figure 1.6: Permittivity (on the left) and conductivity (on the right) variations in skin and their effects on antenna performance are shown. The configuration used in these plots is a patch antenna in contact with the stack of tissues presented in Figure 3.1(b). From these two figures the required accuracy is $\epsilon_r = \pm 1$ and $\sigma = \pm 0.1$ S/m. Thus, phantom tissues measurements require this precision.

A full explanation of making phantom tissues, different validation processes used and final results are presented in Chapter 2.

1.2 Wearable antenna

Currently wearable antennas on the market are used mostly for military purposes, especially for communications. In this scenario, antennas perform in the far field and are often integrated into a garment that the soldier or the person wears. These antennas are designed to interact with the media surrounding the human body, and they are not used for medical or antenna-body applications. Examples of wearable antennas and their applications are shown in Figure 1.7.

Another market is in handsets for mobile communications. These antennas are not designed as wearable antennas, but they operate very close to human tissues, which interfere with the performance of the antenna. It is relevant to mention this scenario because most of the theory applied to wearable antennas comes from the study of handset antennas.

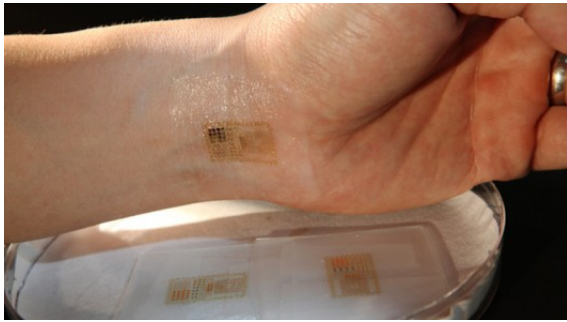
There is much controversy about the possibility of carcinogenesis due to absorption of power radiated by a cell phone in human tissues [47]. Thus, it becomes important to understand the interaction between handset antennas and human tissues. In this thesis, Specific Absorption Rate (SAR), or power absorbed by the tissues, is used as a standard quantity and figure of merit when discussing the antenna-tissue interaction.

Antennas are usually designed to radiate in infinite or semi-infinite free space (assumed to be vacuum). The presence of lossy dielectrics in the near (reactive) field of the antenna significantly affects its performance as shown in Figure 1.8.

If one wants to design an antenna to use in a radiometer and places the antenna directly in contact with human tissues or the human body, one must take into account the performance of the antenna mainly in the near field. In this thesis, different antennas in contact with tissues are investigated, both in terms of the effect of tissues on antenna properties and vice versa. As the main goal of the designed antennas is to capture radiation from the body, studies carried out are focused on propagation of electromagnetic waves through tissues.

Antennas designed in this thesis should have very well defined characteristics, most importantly, the near-field performance characterized by the SAR parameter. This is different than in most antenna applications, where receiver and transmitter are in the far field, i.e. the spherical waveform reaching both could be approximated by a plane wave, where electric and magnetic fields are perpendicular and vibrate transversely to the propagation direction. In a wearable antenna the interaction between antenna and surrounding objects has to be taken into account. This scenario is especially critical in antennas designed to interrogate tissues in direct contact. In addition, standard antenna terminology and methods should be applied with care.

Chapter 3 presents a intensive study of wearable antennas, focusing the study in two very well known antennas dipole and patch antennas.



(a)

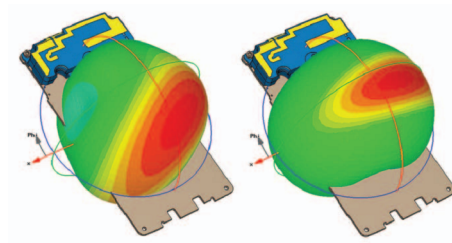


(b)

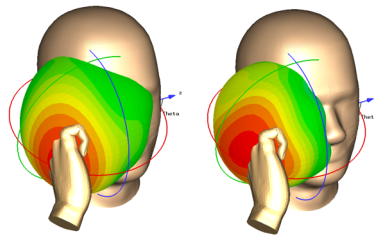


(c)

Figure 1.7: Example of wearable antenna used in military applications, Figure 1.7(a), taken from [7], represents a printed antenna on a person's skin; Figure 1.7(b), taken from [8], shows an antenna integrated on fabric for communications purposes; and Figure 1.7(c), taken from [9], shows different antennas that a soldier might carry in the future on a standard uniform.



(a)



(b)

Figure 1.8: Comparison of the radiation patter of a PIFA antenna designed to be used on a handset for the two GSM bands with and without the presence of the user. On the left the radiation patter of the antenna in free space. On the left the modified radiation pattern in the presence of head and hand. Frequencies are 1 and 2GHz, the antenna is a PIFA antenna used in a Sony-Ericsson handset. Red means high power and green low power. Pictures are taken from [10].

Chapter 2

Phantom tissues

Contents

2.1	Phantom tissues mixing process	20
2.1.1	Procedure for making phantom skin tissues	20
2.1.2	Procedure for making phantom muscle tissues	21
2.1.3	Procedure for making phantom fat tissues	21
2.2	Phantom tissue validation	22
2.2.1	Free space measurements	23
2.2.2	Microstrip based measurements	26
2.2.3	Open-ended coaxial probe	30

In this chapter, a complete process of fabricating and validating phantom tissues is presented. Phantom tissues are developed to validate antenna results presented in chapter 3. These tissues will be used along with the designs presented in chapter 3 to model the human body and validate the simulations.


The goal behind producing these mixtures is to mimic electrical properties of real tissues at microwave frequencies, from hundreds of megahertz to gigahertz. Three different tissues are generated (skin, fat and muscle) and layered to simulate the generic configuration of the body's surface.

2.1 Phantom tissues mixing process

Phantom tissues are mixtures of mostly pure water, oil and salt. In addition propanol, agarose powder and soap are used. Skin and muscle phantom tissues mixtures are developed, following the recipes of Topsakal '08 [41], but adapting this published process using several other publications [42, 43, 44, 45, 46]. The technique presented here uses equipment common to any RF lab and is detailed in this section.

Two methods are presented and tested for skin and muscle mixtures. A third method was developed with unsuccessful results for a fat phantom. A photograph of the final mixtures are shown in Figure 2.1.

2.1.1 Procedure for making phantom skin tissues

- (1) Heat 45 ml of pure vegetable oil to 80 °C in a 100 ml beaker.
- (2) Slowly heat a solution of 65 ml of water and 1.33 grams of agarose powder in a separate 100 ml beaker.
- (3) Turn off the heat and mix in 0.4 grams of NaCl salt and 1.68 ml of  Ultra Ivory dish soap to the water solution when it begins to release steam and use the hand blender to mix the solution thoroughly.
- (4) Add the oil (heated to 100 °C) and the water solution to a third beaker by alternately adding a small amount of each and stirring constantly.
- (5) If desired, add a drop of food coloring to the new mixture, in order to easily keep track of different mixtures.
- (6) Using a hand blender, blend the solution in the third beaker thoroughly until the mixture becomes homogenous.

- (7) Quickly pour the mixture into the desired mold and allow it to gelatinize overnight at room temperature

2.1.2 Procedure for making phantom muscle tissues

- (1) Heat 30 ml of pure vegetable oil to 80 °C in a 100 ml beaker.
- (2) Slowly heat a solution 60 ml of water and 1.33 grams of agarose powder in a separate 100ml beaker.
- (3) Mix in 0.4 grams of NaCl salt and 1.68 ml of $\text{\textcircled{R}}$ Ultra Ivory dish soap to the water solution when it begins to release steam and use the hand blender to mix the solution thoroughly.
- (4) Add the heated oil and the water solution to a third beaker by alternately adding a small amount of each and stirring constantly.
- (5) If desired, add a drop of food coloring to the new mixture, in order to easily keep track of different mixtures.
- (6) Using the hand blender, blend the solution in the third beaker thoroughly until the mixture is homogenous.
- (7) Pour the mixture into the desired mold and allow it to solidify overnight at room temperature

2.1.3 Procedure for making phantom fat tissues

- (1) Mix 0.2 g of p-toluic acid powder with 10 ml of propanol and stir vigorously until it the powder has completely dissolved.
- (2) Heat 800 ml of pure vegetable oil to 80 °C in a beaker.
- (3) Mix the solution made in (1) to 190 ml of water and heat the new solution to 80 °C.

- (4) Mix the heated oil and heated water solutions and add 11.2 ml of $\text{\textcircled{R}}$ Ultra Ivory dish soap. Use the hand blender to emulsify this solution. The solution should turn white with very little foam.
- (5) If desired, add a few drop of food coloring to the new mixture, in order to easily keep track of different mixtures.
- (6) Using the hand blender, blend the mixture thoroughly a final time.
- (7) Quickly pour the mixture into the desired mold and allow it to gelatinize overnight at room temperature.
- (8) NOTE: If the procedures described for fat do not yield a well-gelatinized material, try using smaller proportions of materials. We used 1/5th of the quantities above for the results reported here.

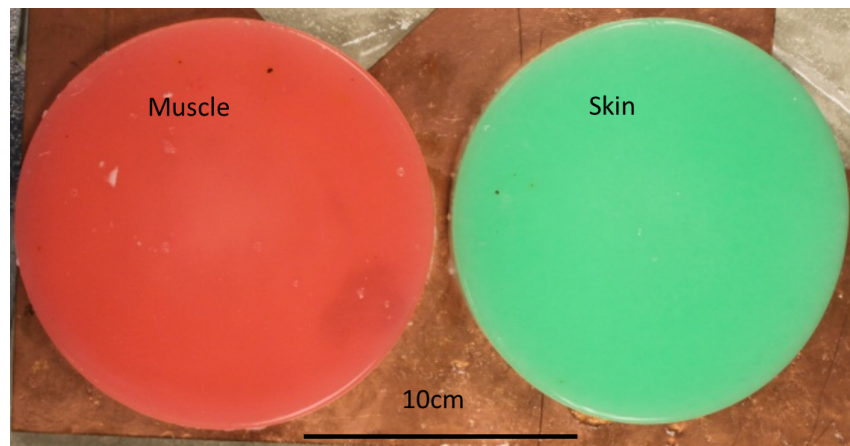


Figure 2.1: Photo of skin (green) and muscle (red) final mixtures

2.2 Phantom tissue validation

Phantom tissues are created to have the same electrical properties as human tissues. In order to validate our phantom tissues after the mixing process, we measured the electrical

properties defined by complex permittivity. Permittivity is defined by equation 1.5 and explained in section 1.1.1. Techniques to measure these properties are explained in section 1.1.3.1.

Different techniques were used to measure electrical properties of tissues. These techniques were chosen because: (1) the phantom tissues are gummy and oily materials and when manipulated leave some residues; and (2) they are not solid and cannot be cut in to perfect shapes. These two issues restrict the viable techniques available to measure permittivity. For example, when using a resonant cavity, as presented in different publications, e.g. [48, 49, 50], to measure permittivity of phantom tissues, the sticky residue may ruin the chamber for future uses. Other techniques unsuitable for measuring phantom tissues are waveguide or coaxial-based techniques, where the allocated space for the dielectric is filled with the phantom tissue material. The problem with these techniques is the quality of the contact between the conductive walls and the Material Under Test (MUT). Phantom tissues will not have perfect contact with the walls, introducing error due to placing air bubbles. In the literature, e.g. [51] or [14], the contact with a coaxial probe or the conducting wall and the MUT is discussed and shows that insufficient contact will introduce underestimation of the material electrical properties. Thus, it is important to use techniques where these effects are reduced or canceled. In the open-ended coaxial probe, this effect can be reduced, but not canceled, by applying pressure between the probe and the MUT. Detailed explanation will follow in the next section. First describing a free space and a microstrip-based method and concluding with the discussion of an open-ended coaxial probe method which we believe is the most accurate. Here it is important to mention that the microstrip method proposed here was presented at the International Union of Radio Science (URSI) meeting [52].

2.2.1 Free space measurements

Free space measurement (Figure 2.2) uses waves propagating in free space that interact with the Material Under Test (MUT). This technique is non-destructive and does not

require contact with the sample. A disadvantage of the technique is that at lower microwave frequencies it requires an electrically large, flat and uniform sample.

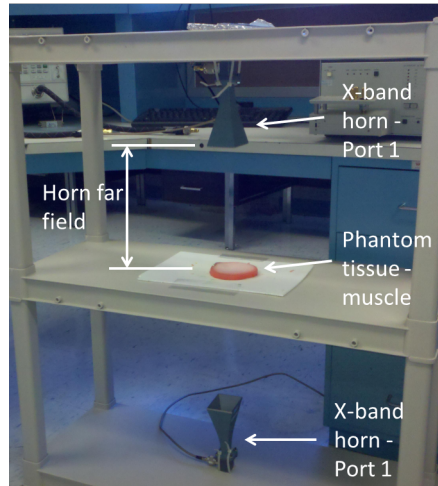


Figure 2.2: Free space measurement setup, with phantom muscle tissue between the two antennas connected to the VNA. As shown, the two antennas are the two ports used. The two antennas must be at least at the far field distance from the tissues.

The setup consists of two antennas connected to a network analyzer, where the MUT is placed (Figure 2.2) between the antennas and in the far field of both antennas. The setup is critically dependent on the beam-sample interaction and, for a simple transmission line model, high directivity antennas or big sample are required. It is recommended that the sample fills inside the HPBW (Half-Power Beamwidth) angle. At this point it is interesting to comment on some solutions applied to minimize the error introduced by of the beam-sample interaction. There are two obvious solutions: using lenses to focus the beam or placing the sample in an absorber. At microwave frequencies, lenses are very large (50 cm in diameter at X-band) making the measurements not practical. The approach with the absorptive aperture involves developing a new calibration technique.

If a large enough sample can be made, the equivalent circuit shown in Figure 2.3 is valid, otherwise some edge effects are introduced and there will be an error in the measurements.

The main source of error is diffraction which is also makes calibration process difficult.

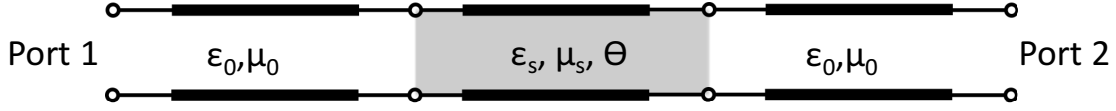


Figure 2.3: Free space measurements technique equivalent transmission model. The ports represent the two antennas shown in Figure 2.2.

There are three ways to calibrate these two port measurements: Thru-Reflect-Match (TRM), [53]; Thru-Reflect-Load, [54]; and Gated SOLT, [55].

The third method is proposed by Agilent in the free space measurements seminar [55]. This calibration uses time domain gating. The first step is to calibrate the system at the end of the cables that will be connected to the antenna, using normal calibration procedures (SOLT). Then, the antennas are connected and the network analyzer is switched to time domain, in order to be able to measure distances. A metal plate is placed at the reference plane of the sample and a time domain analysis is applied to reduce the error introduced by the surrounding environment. The metal plate must have approximately the same thickness as the material that will be measured; otherwise, the window will include some free space or will exclude the sample.

A common method to extract permittivity parameters from the measurements is the Nicholson-Ross method [56] and [57]. This method assumes the sample is completely inside a guiding medium (shown in Figure 2.3), and no waves are propagating through any other material but the sample. Obviously, if the sample does not fill the domain, an error will be introduced. Permittivity and permeability may be extracted from two complex value measurements (S_{11} and S_{21}) as follows. First we define new complex variables:

$$V1 = S_{21} + S_{11}; V2 = S_{21} - S_{11} \quad (2.1)$$

from there, we define:

$$z = \frac{V1 - \Gamma}{1 - V1 * \Gamma}; \Gamma = X \pm \sqrt{X^2 - 1}, \Gamma \leq 1; X = \frac{1 - V1V2}{V1 - V2} \quad (2.2)$$

$$c_1 = \left(\frac{1 + \Gamma}{1 - \Gamma} \right)^2; c_2 = - \left(\frac{c}{\omega d} \ln \left(\frac{1}{z} \right) \right)^2 \quad (2.3)$$

c_1 and c_2 are complex numbers and functions of the real and imaginary parts of S_{11} and S_{21} . From here, complex relative permeability and permittivity can be found according to [56]:

$$\mu = \sqrt{(c_1 c_2)}; \epsilon = \sqrt{(c_1 / c_2)} \quad (2.4)$$

A significant effort was put into this measurement technique, but unfortunately because of the size and uniformity of the sample and large wavelength of interest (a few gigahertz), it was difficult to obtain results with any accuracy. Therefore a different guided wave technique was investigated next, microstrip-based measurements.

2.2.2 Microstrip based measurements

The idea behind this measurement is to use a calibrated microstrip fixture and TRL calibration. The Thru-Reflect-Line calibration consists of six complex measurements which result in an overdetermined system of equations, a detailed explanation of which is given in [54] and [58]. Therefore, in addition to the four complex scattering parameters, either the complex propagation constant or the complex impedance of the reflection standard can also be found at every frequency. The sketch of a cross section of a microstrip line on a lossless substrate with a lossy (phantom tissue) superstrate is shown in Figure 2.4. The impedance and propagation constant of the microstrip line are affected by the presence of the superstrate. By measuring S-parameters and using multiple linear regression one may extract complex permittivity using very well-defined response characteristics.

A flowchart of the process is shown in Figure 2.5.

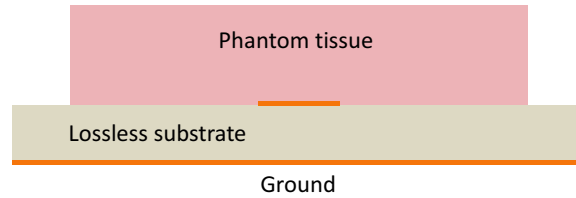


Figure 2.4: Cross section of the microstrip fixture with the lossy material on top.

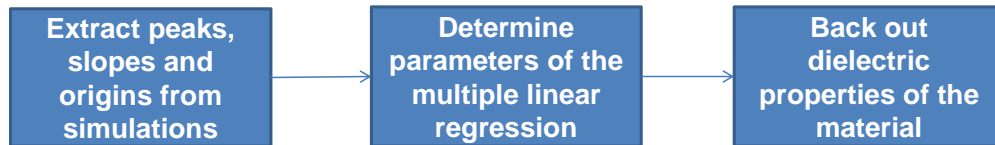


Figure 2.5: Flowchart of method used to extract superstrate electrical properties

The first step to define the response characteristics is to specify the required accuracy. From Figure 1.6 a reasonable specification is determined to be:

- Dielectric constant accuracy : $\Delta\epsilon=1$
- Conductivity accuracy: $\Delta\sigma=0.1$

As a reminder, Figure 1.6 presents simulations of antennas of phantom tissue models and determines the required accuracy for the tissue parameters in order to obtain reasonable antenna models.

Next, full wave simulations (HFSS) were performed for the calibration standards with the range of relative permittivity between 5 and 60, a conductivity of 1S/m, and a range of conductivity of 0.5 to 1.6S/m for relative permittivity of 10. The simulations results are shown in Figures 2.6, 2.7 and 2.8. For each value of ϵ_r, σ was varied. Only a selection of curves is shown in the plots.

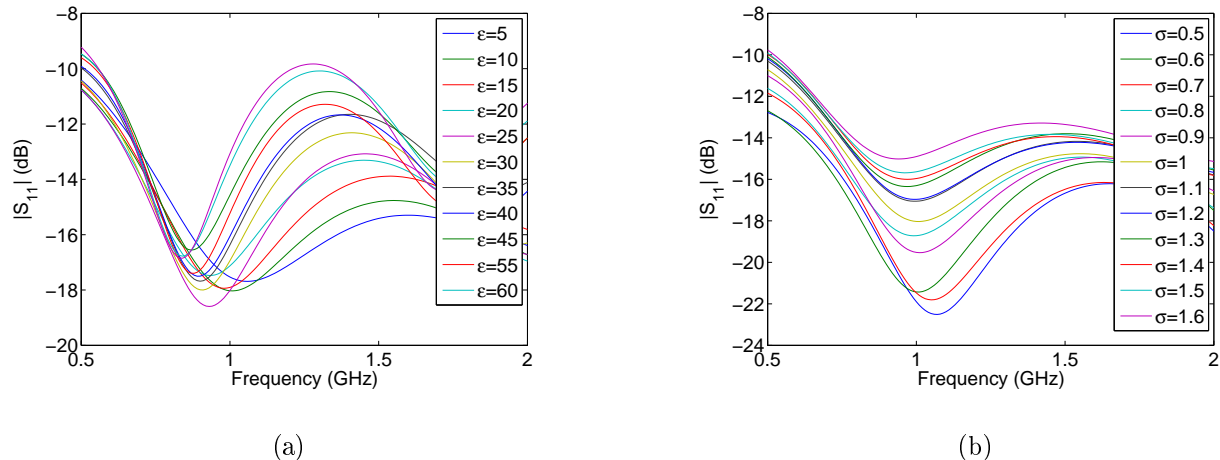


Figure 2.6: Simulations performed for the Thru microstrip standard. 2.6(a) with sigma 1S/m epsilon relative varied between 5-60 and the resulting amplitude of S_{11} is shown. 2.6(b) with epsilon 10 sigma varied between 5-60 and the resulting amplitude of S_{11} is shown.

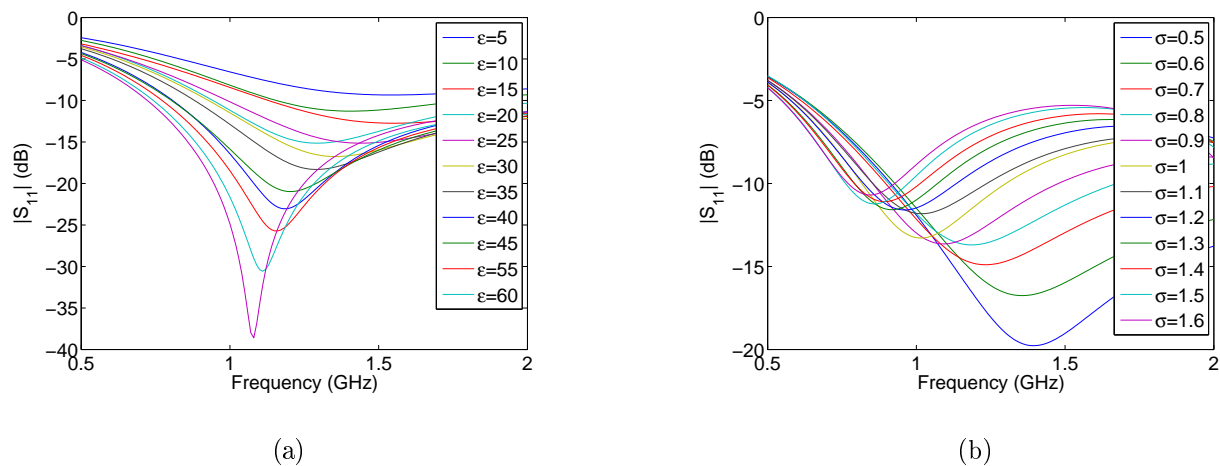


Figure 2.7: Simulations performed for the Reflect microstrip standard. 2.7(a) with sigma 1S/m epsilon relative varied between 5-60 and the resulting amplitude of S_{11} is shown. 2.7(b) with epsilon 10 sigma varied between 0.5-1.6S/m and the resulting amplitude of S_{11} is shown.

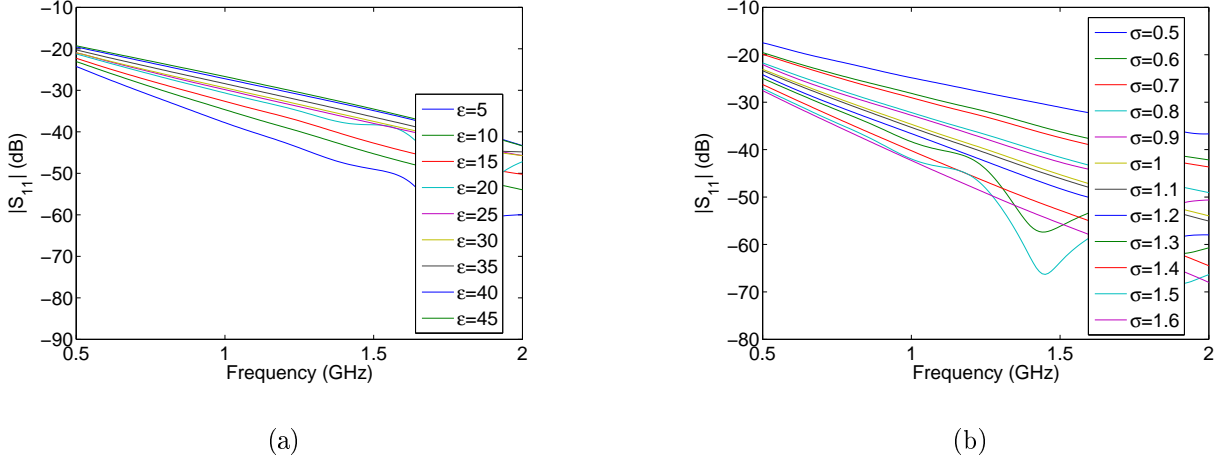


Figure 2.8: Simulations performed for the Thru microstrip standard. 2.8(a) with sigma 1s/m epsilon relative varied between 5-60 and the resulting amplitude of S_{21} is shown. 2.8(b) with epsilon 10 sigma varied between 5-60 and the resulting amplitude of S_{21} is shown.

From the reflection standard, the S_{11} minimum is extracted and from the Thru and Line simulations the origin value and the slope are extracted. Very well-defined characteristics should be extracted and those are the clearest characteristics of each standard. Moreover, it is important to mention that phase does not have very well-defined characteristics, thus phase is unsuitable to be used in this method.

Let the variable values extracted from the simulation be the matrix X and the related permittivity be represented by a matrix Y defined as follows:

$$X = \begin{pmatrix} x_{11} & \dots & x_{1p} \\ \vdots & \ddots & \vdots \\ x_{n1} & \dots & x_{np} \end{pmatrix}; \quad Y = \begin{pmatrix} y_1 \\ \vdots \\ y_n \end{pmatrix} \quad (2.5)$$

where:

$$y_i = \beta_1 x_{i1} + \dots + \beta_p x_{ip} + \varepsilon_i \quad (2.6)$$

$$Y = \beta X + \varepsilon \quad (2.7)$$

with:

$$\beta = \begin{pmatrix} \beta_1 \\ \vdots \\ \beta_p \end{pmatrix}; \quad \varepsilon = \begin{pmatrix} \varepsilon_1 \\ \vdots \\ \varepsilon_p \end{pmatrix} \quad (2.8)$$

where ε and β are constants calculated from while X and Y, meanwhile X and Y are extracted from measurements.

The advantage of this method is that different media, such as microstrip, stripline or coplanar waveguide could be used in conjunction with TRL calibration. The disadvantage of the method became apparent during the experiments as it was difficult to obtain repeatable results because of the contact of the MUT and the microstrip line. In addition, the Line and Thru standards need to be longer than λ , where λ is the wavelength at the lowest frequency, making it difficult to go to lower frequencies with available fixtures and samples. Another disadvantage is that the sample has to be thin with uniform thickness which is difficult to implement. The author asserts that the method is better for less conductive materials. A recommendation is to look at the effect of a different dielectric constant of the lossless substrate on the accuracy of the extraction.

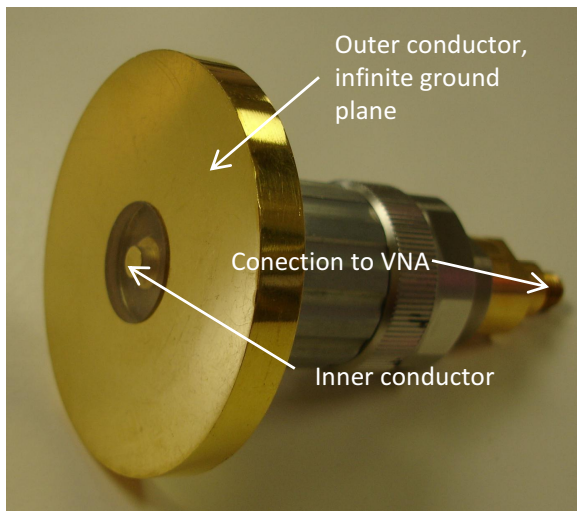
This method was presented at the URSI conference 2012 [52].

2.2.3 Open-ended coaxial probe

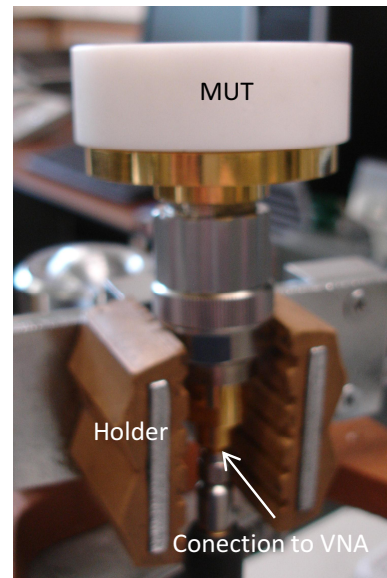
Open-ended coaxial probes (shown in Figure 2.9) are widely used in measuring dielectric properties of materials at microwave frequencies. The method is noninvasive and nondestructive and thus well-suited for measurements of biological materials. Using this method, one may achieve measurements of dielectric relaxations for a wide spectrum of frequencies, which is essential for biological tissues because one may measure the important resonances that characterize these materials.

The main characteristics defining this method are:

- Nondestructive and noninvasive for the material/sample under test (MUT). The tested material could be kept intact and no cutting or reshaping is needed. Other methods, especially resonant methods, require specific sample dimensions;
- Broad frequency range, limited by probe dimensions;
- The precision is intermediate to low, achieving precisions $<10\%$, [59];
- No frequency sampling constraints. Resonant methods allow measurements at only a few frequencies; the open-ended coaxial method does not have this limitation. The frequency sampling limitation comes only from the instrumentation used.



(a)



(b)

Figure 2.9: Open-ended coaxial probe used at the National Institute for Standards and Technology. The probe has different dimensions depending of the frequency range of interest. Figure 2.9(a) shows the probe. Figure 2.9(b) shows the probe with the MUT on top. In our case the tissue material was not firm, so it was placed under the probe. Courtesy: Dr. Michael Janezic, NIST Boulder

The open-ended coaxial probe uses the effect of the sample on the fringing fields at the end of the probe. When there is no sample, the cable is just in contact with air, the field lines bend from the outer conductor to the inner conductor and ideally spread to infinity. When the sample is placed at the very end of the probe, affects the fringing fields directly, changing the reflection coefficient. A lossy capacitor is the best way to model this variation in the fringing fields. An equivalent circuit of this method is shown in Figure 2.10.

The method is widely discussed in the literature, and its limits are well known, e.g. Athley and Stuchly 1982 [30], Grant 1989[16], Baker-Jarvis 1994 [51], Dong 2009 [60] and Elison [61].

2.2.3.1 Calibration

There are different ways to calibrate the system. The most widespread calibration method is SOLT calibration [62]. SOLT calibration uses three standards: Short, Open and Load for one port calibrations. There are two ways to apply the SOLT calibration to the probe. The first one is by calibrating the system at the end of the cable connected to the network analyzer using the usual kit with the three standards. Then, an algorithm has to be used to de-embed the distance between the reference plane at the end of the cable and the open-ended probe. A second method is to use the SOLT calibration directly at the end of the probe. This calibration consists of Short, which is just a short circuit between the inner and the outer conductor of the probe; Open, with the probe open to air and finally Load , which is simply applying a load at the end of the probe. Most common loads used are reference liquids with well known dielectric properties. Reference liquids are discussed in [63] and [64].

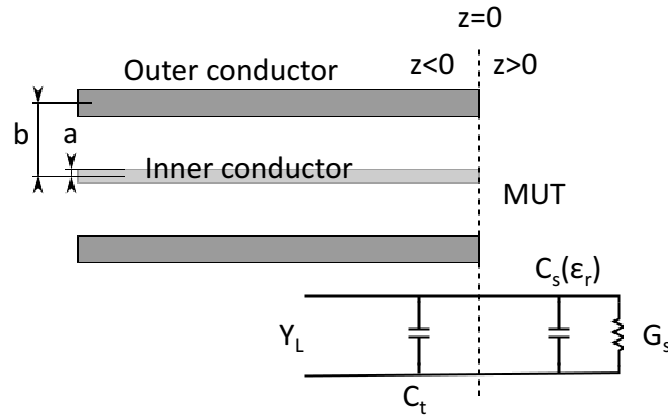


Figure 2.10: Equivalent circuit of the open-ended coaxial probe, where the material is modeled as a capacitor and a resistor in parallel denoting the real and imaginary part of the permittivity

2.2.3.2 Extraction of admittance models at the end of the open ended coaxial probe

This method is based on extracting the reflection coefficient at the termination of the probe:

$$\Gamma = \frac{Z_n - Z_0}{Z_n + Z_0} \quad (2.9)$$

where Z_0 is the characteristic impedance of the coaxial line and Z_n is the characteristic impedance of the unknown material.

As shown in figure 2.10, the equivalent circuit consists of two capacitors and a resistance in parallel, so it is easier to work using admittances.

Some assumptions are taken when calculating the admittance at the end of the probe:

- MUT is homogeneous and occupies the half space beyond the probe
- The ground plane is theoretically infinite; in practice it is large enough to cover most of the energy of the system.

There are two methods to extract the MUT dielectric properties. The first one is using lumped element equivalent circuit explained in section 2.2.3.2, and the second is calculating the fields coming out from the probe, called the Point Matching Method, explained in 2.2.3.2. The first one is easier but less accurate, and requires to define the capacitance of the probe (C_s in Figure 2.10) which is not simple. The second method consists of calculating the magnetic fields at the end of the probe coupled with the MUT. This results in an equivalent admittance and finally a reflection coefficient. All these equations depend on the permittivity. By repeating the process in reverse, one can find the electrical properties.

Lumped element method

This method uses the equivalent circuit shown in Figure 2.10. To extract the dielectric properties of the MUT, the reflection coefficient has to be measured, the output impedance calculated and the equivalent capacitance and resistance extracted. From there the complex permittivity can be extracted. The output impedance (admittance) of the equivalent circuit shown in Figure 2.10 is as follows:

$$Y_L = Y_0 \frac{1 - \Gamma}{1 + \Gamma} = j\omega C_t + j\omega C_s + G_s \quad (2.10)$$

where $C_s = C_s(\epsilon_r)$. The related reflection coefficient is given by:

$$\Gamma = |\Gamma| e^{j\varphi} = \frac{1 - j\omega Z_0 [C_s + C_t]}{1 + j\omega Z_0 [C_s + C_t]} \quad (2.11)$$

where the capacitance and conductance of the sample (C_s and G_s) are included in $C'_s(\hat{\epsilon})$ which is a capacitor with a complex permittivity dielectric. From here the complex permittivity may be finally extracted using:

$$\hat{\epsilon} = \frac{1 - \Gamma}{j\omega Z_0 C_s [1 + \Gamma]} - \frac{C_t}{C_s} \quad (2.12)$$

where $\hat{\epsilon}$ is related to the capacitance and resistance in parallel on the equivalent circuit. The real part of $\hat{\epsilon}$ is related to the capacitance and is extracted from:

$$\epsilon' = \frac{-2\Gamma \sin \varphi}{\omega Z_0 (1 + |\Gamma| \cos \varphi + |\Gamma|^2)} - \frac{C_t}{C_s} \quad (2.13)$$

and the imaginary part of $\hat{\epsilon}$ is related to the parallel resistance and is extracted from:

$$\epsilon'' = \frac{1 - |\Gamma|^2}{\omega Z_0 (1 + |\Gamma| \cos \varphi + |\Gamma|^2)} \quad (2.14)$$

where $|\Gamma|$ is the magnitude, φ is the phase of the reflection coefficient and Z_0 is the characteristic impedance of the line. Both real and imaginary impedance could be modeled as an equivalent capacitance with a dielectric with complex permittivity.

The equivalent circuit is valid at frequencies where the dimensions of the line are small compared to the wavelength. That is, the open end of the line is not radiating and all the energy is concentrated in the reactive near field of the line where the sample is placed.

MUT-probe contact is critical for these measurements. If the contact is not optimal, the measurements will underestimate the complex permittivity [51, 14]. Thus, different techniques are used to improve contact by avoiding air gap formation. One of such techniques is to apply a layer of vegetable oil or water between the probe and sample. In addition, pressure through the cable can also be applied to avoid the same problem.

The same system may be used to measure complex permittivity of liquids. For this purpose, a small container with a small amount of the liquid is used. The measurements used are the same, and no moistening or pressure is required because it is easy to have good contact. This configuration applied to blood measurements is sketched in Figure 2.11.

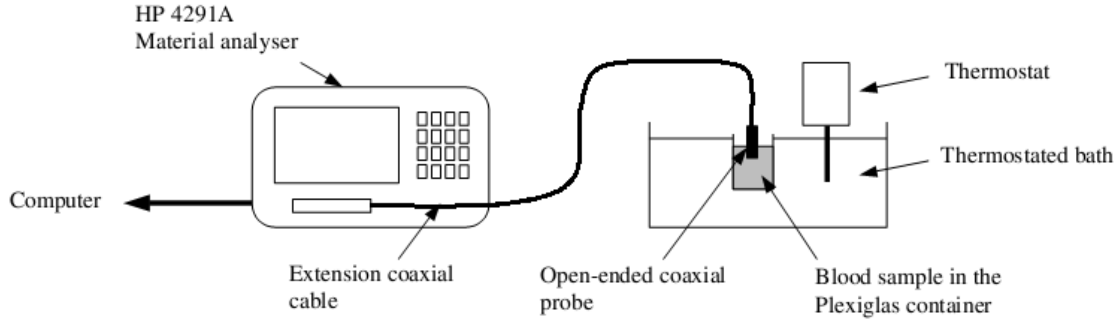


Figure 2.11: Open-ended coaxial probe used to measure liquid dielectric properties. The system has a thermostat bath that allows temperature measurements. The sketch shows the system for blood measurements and is taken from [11].

It is important to note that this method is based on two approximations: it assumes uniform permittivity and no radiating effects. The probe dimensions determine the frequency limit of the method according to the $2b/\lambda \ll 1$ limiting relation, where b is the inner diameter of the outer conductor.

In order to use the lumped element method, coefficients C_s and C_t stated in Equation 2.12, may be measured using reference materials with known electrical properties at the same temperature. [64] and [63] include a list of different publications where data for different materials are listed.

Extracting C_s and C_t is not a straightforward process and is discussed in [16]. Up to about 1GHz, where only a TEM mode is above the cutoff, the following equations can be used to find C_s from a known material:

$$C_s = \frac{1}{\omega Z_0 (\epsilon'^2 + \epsilon''^2)^{1/2}} \quad (2.15)$$

$$\frac{-2|\Gamma| \sin \varphi}{\omega Z_0 (1 + |\Gamma| \cos \varphi + |\Gamma|^2)} = C_s \epsilon' + C_t \quad (2.16)$$

where ϵ' and ϵ'' are the real and imaginary part of the known complex material permittivity.

Meanwhile previous relations are perfectly valid up to 1GHz, for higher frequencies some discrepancies are observed because the principal TEM mode becomes supplemented by evanescent TM modes excited at the junction, [65]. This leads to use non linear equation as follows:

$$C_s(f, \hat{\epsilon}) = C_s + Af_e^2(\hat{\epsilon}) \quad (2.17)$$

where $f_e(\hat{\epsilon})$ is an effective frequency calculated as follows:

$$f_e(\hat{\epsilon}) = \frac{c}{\lambda_0} \left\{ \frac{\epsilon'}{2} \left[\left(1 + \frac{\epsilon''}{\epsilon'} \right)^{1/2} + 1 \right] \right\}^{1/2} \quad (2.18)$$

Thus:

$$C_s(f, \hat{\epsilon}) = \frac{-2|\Gamma| \sin \varphi}{\omega Z_0 \epsilon' (1 + |\Gamma| \cos \varphi + |\Gamma|^2)} - \frac{C_t}{\epsilon'} \quad (2.19)$$

As frequencies of interest in this thesis are below 2GHz, the linear method is used.

Point matching method

This method was presented in [15] and consists of extracting the electric properties through the values of the reflection coefficient. The reflection coefficient is expressed in a general form for a general complex permittivity and this complex value can be extracted from the measured reflection coefficient.

In Figure 2.12 the coordinate system used is shown. The process followed is as follows:

- extract the electric and magnetic fields on the coaxial line, from [66] and [67]:

$$E_\rho = U_0 \left[f_0(\rho) \exp(-\gamma_0 z) + \sum_{n=0}^{\infty} \mathbf{R}_n f_n(\rho) \exp(\gamma_n z) \right] \quad (2.20)$$

$$H_\phi = j\omega\epsilon_0\epsilon_c U_0 \left[\frac{f_0(\rho)}{\gamma_0} \exp(-\gamma_0 z) - \sum_{n=0}^{\infty} \mathbf{R}_n \frac{f_n(\rho)}{\gamma_n} \exp(\gamma_n z) \right] \quad (2.21)$$

where $f(\rho)$ is defined in terms of the probe dimensions, the eigenvalues p_n and the coordinate ρ , detailed explanation is given in [15]; \mathbf{R}_n is the general reflection coefficient of

the mode n ($R_0 \equiv \Gamma$), U_0 is an arbitrary amplitude factor, and the propagation factor of the mode n is given by: $\gamma_n = [p_n^2 - \epsilon_t (\omega/c_0)^2]^{1/2}$ where c_0 is the speed of light in free space. Moreover, the radial function is a function of the probe dimensions, b and a , the inner and the outer conductor dimensions and the eigenvalues p_n . Finally, assume continuity of the electric field at the interface that leads to the continuity of the magnetic field:

$$\mathbb{H}_\phi(\rho, z = 0^-) = \mathbb{H}_\phi(\rho, z = 0^+) \quad (2.22)$$

leads to equation 2.23:

$$\sum_{n=0}^{\infty} \mathbf{R}_n \mathbf{T}_n = 1 \quad (2.23)$$

where an infinite plane is assumed, so $0 < \rho < \infty$, and:

$$\mathbf{T}_n = \frac{f_n(\rho)/\gamma_n + (\epsilon_s/\epsilon_t) \mathbf{I}_n}{f_0(\rho)/\gamma_0 - (\epsilon_s/\epsilon_t) \mathbf{I}_0} \quad (2.24)$$

in which

$$\mathbf{I}_n = \frac{1}{2\pi} \int_b^a \int_0^{2\pi} f_n(\rho') \rho' \frac{\exp(-j(\omega/c_0)\sqrt{\epsilon_s}r)}{r} \cos \psi d\rho' d\psi \quad (2.25)$$

Since the summation in Equation 2.23 goes to infinity, it is important to truncate it to be useful in real methods or measurements. Since these equations use magnetic fields, and high order modes are evanescent, the terms decrease rapidly as n increases, making the summation go from 0 to N , shown in Equation 2.26. In some publications only $N \sim 5$ is used [16], giving the final relation:

$$\sum_{n=0}^N \mathbf{R}_n \mathbf{T}_n = 1 \quad (2.26)$$

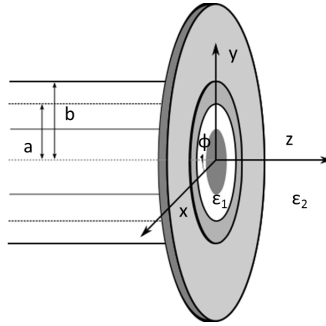


Figure 2.12: Coordinate system used. Subscripts 0, 1 and 2 denote air, dielectric inside the coaxial line and dielectric outside the coaxial line, respectively

2.2.3.3 Results

The first step before measuring is to simulate the system in order to know what the results should look like and compare them against previous publications. In this thesis, the lumped element method is used to extract complex permittivity of the materials used in simulations and the matching point method is used to extract the same properties from measured materials.

The first method requires measuring and extracting the values of C_s and C_t from reference materials. Extraction of these coefficients is not trivial as previously explained. In Grant '89 [16] full discussion of C_s and C_t extraction is included.

Using the point matching method, an algorithm capable of extracting the MUT complex permittivity has to be used. The algorithm has to find the permittivity and conductivity that lead to the measured reflection coefficient (magnitude and phase) using equations stated in the previous section.

In Figure 2.13 there are plots of reference material used in the literature ([15, 12, 13, 14]) comparing simulations made in this thesis with the publications' results. These are included in order to validate the simulations, presenting reflection coefficient magnitude and phase.

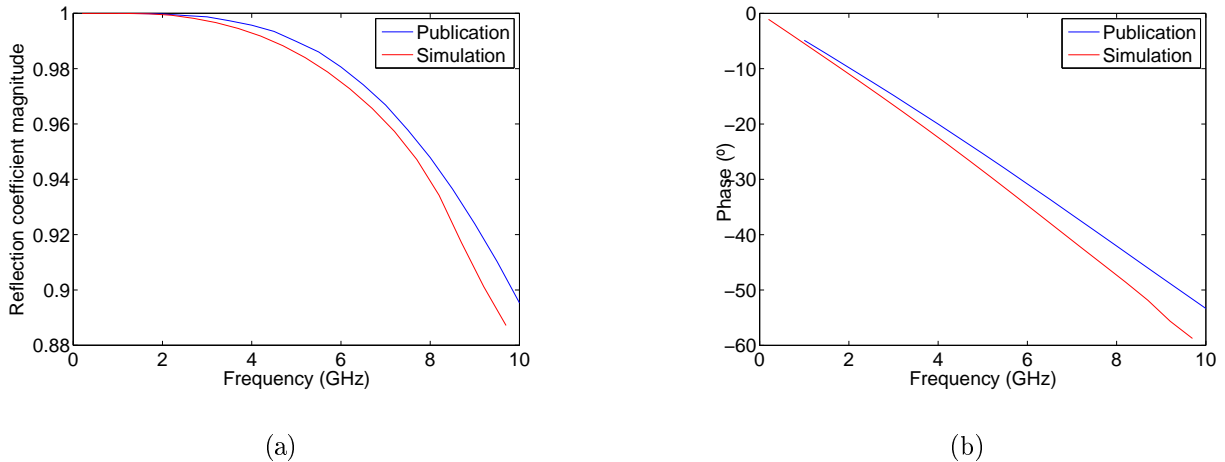


Figure 2.13: Results of simulations for material ($\epsilon = 2.05$) with material used in the literature ([12, 13, 14]) and extracted from [15]. In the simulation the cable connecting the probe and the source has some length but in the previously mentioned publication [16] it has no length. A small shift to lower values is observed, mainly because of the length of the coaxial probe.

Extraction of C_s and C_t coefficients from simulations and for our specific probe

In Figure 2.14, the plot to extract C_s value is shown. The final goal is to extract the electrical properties of phantom tissues up to 2GHz or lower. Thus, to extract C_s and C_t values, one may use Equation 2.19 with known permittivity values. In the simulations, higher frequencies are shown, and the materials used are Methanol, Ethanol, Water and Propanol-1-ol. Cole-Cole model values for these materials are extracted from [16] and shown in Table 2.1.

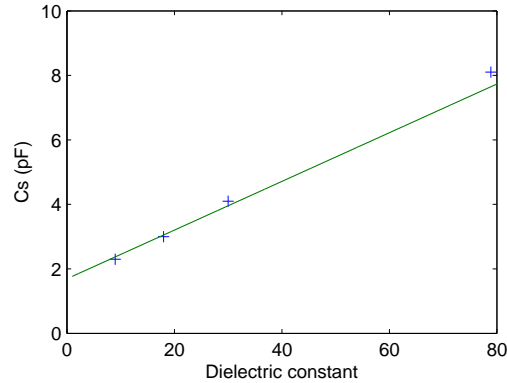


Figure 2.14: C_s extraction curve from reference materials listed in [16]. Solid line is least-squares fit of the sample capacitance measured for known materials (blue cross).

To validate these values, one may extract from previous simulations (Figure 2.13(a) and 2.13(b)) the value of the dielectric constant of this material. Results are shown in Figure 2.15. The reference material has a uniform dielectric constant of 2.05 and no significant conductivity. Simulations lead to a slightly lower final permittivity. This could be due to the length of the cable used in the simulations. The length of the cable affects the value of the reflection coefficient phase. As this length could not be zero for practical reasons on the simulation, the shortest possible length is chosen. The cable length is 0.1mm and it could introduce some phase delay leading to these shifted values. Higher frequencies are more sensitive to the cable length phase delay, due to their lower wavelength. Therefore, as the error increases with frequency, one may think the main problem of the simulations results is the cable length.

<i>Reference liquid</i>	<i>Cole-Cole parameters</i>	<i>Value</i>
Methanol	ϵ_s	33.7
	ϵ_∞	4.4
	f_r (GHz)	3.22
	α	0.36
Ethanol	ϵ_s	24.4
	ϵ_∞	4.8
	f_r (GHz)	1.14
	α	0.0
Water	ϵ_s	78.3
	ϵ_∞	4.6
	f_r (GHz)	19.7
	α	0.014
Propanol-1-ol	ϵ_s	20.6
	ϵ_∞	4.2
	f_r (GHz)	0.52
	α	0.0

Table 2.1: Reference materials used to extract C_s and C_t parameters.

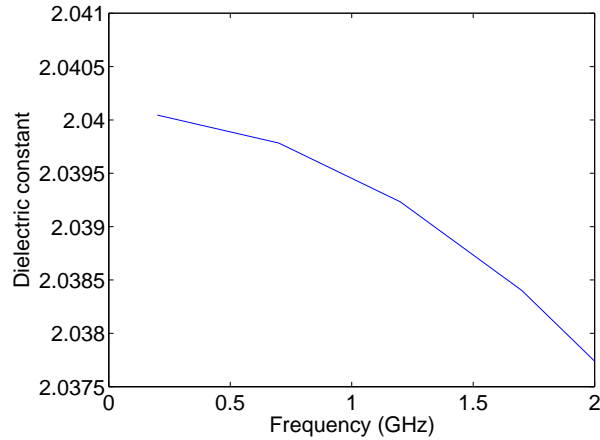


Figure 2.15: Dielectric constant of reference material ($\epsilon_r = 2.05$) used to extract required parameters C_s and C_t and to validate simulations.

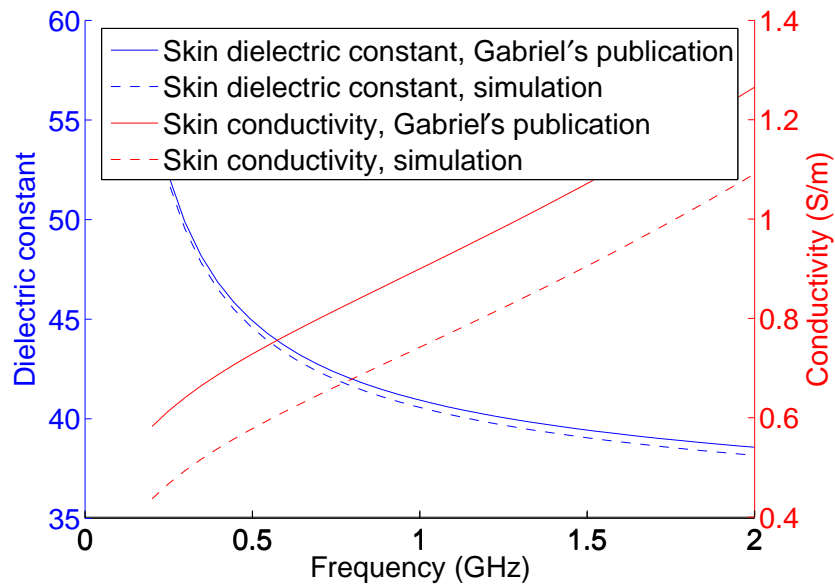
Simulation results

Simulations are carried out for the two types of tissues mixed, skin and muscle. Skin simulation results are shown in Figure 2.16(a). Muscle simulation results are shown in Figure 2.16(b). In both cases results show lower values for dielectric constant and conductivity. Permittivity results show an increasing discrepancy with frequency. Conductivity values show a constant shifting to lower values over the frequency range. Lower values could be explained by the cable length discussed previously.

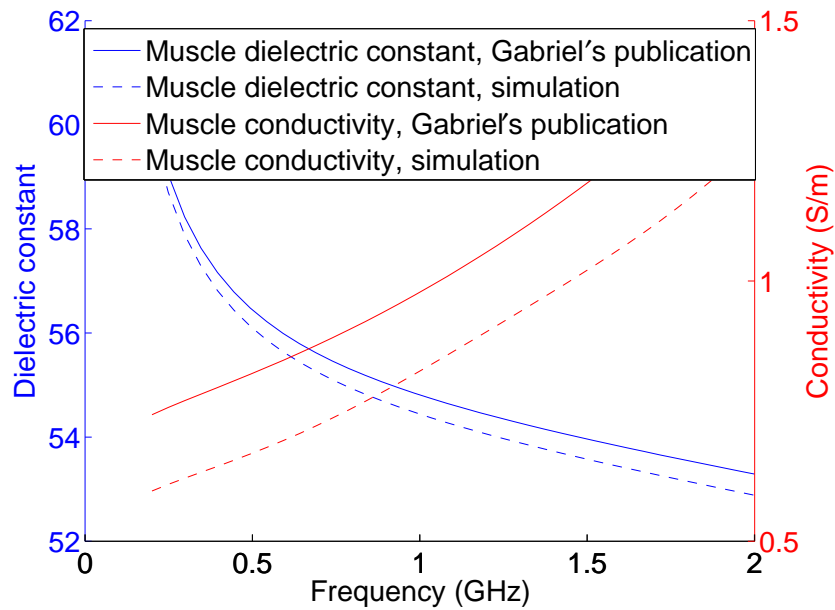
Measurements results

Measurements of the phantom tissues using the open-ended coaxial probe were carried out at NIST (National Institute of Standards and Technology) along with Dr. Michael Janezic using the matching point method to extract complex permittivity values.

The method used consisted of calibrating the VNA at the end of the coaxial cable attached to the probe using a typical SOLT calibration. To extract MUT complex permittivity, the reference plane had to be shifted to the end of the probe. Then, an algorithm is used to move the reference plane and extract the permittivity values using the process explained in section 2.2.3.2.

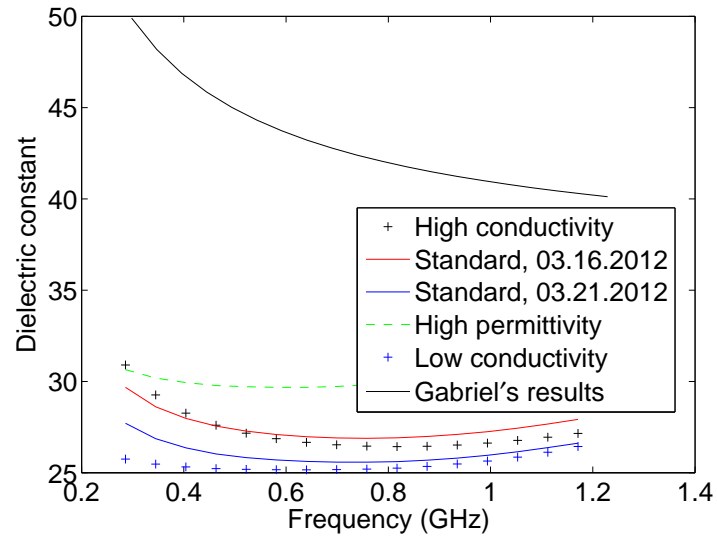


(a)

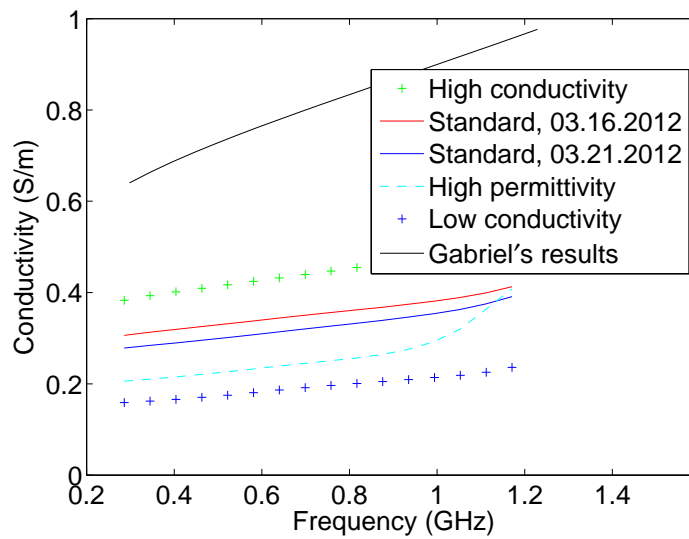


(b)

Figure 2.16: Results of simulations for skin (top) and muscle (bottom). The permittivity is plotted in blue and the conductivity is plotted in red. Solid lines are from Gabriel's publication and dashed lines are results from simulations.

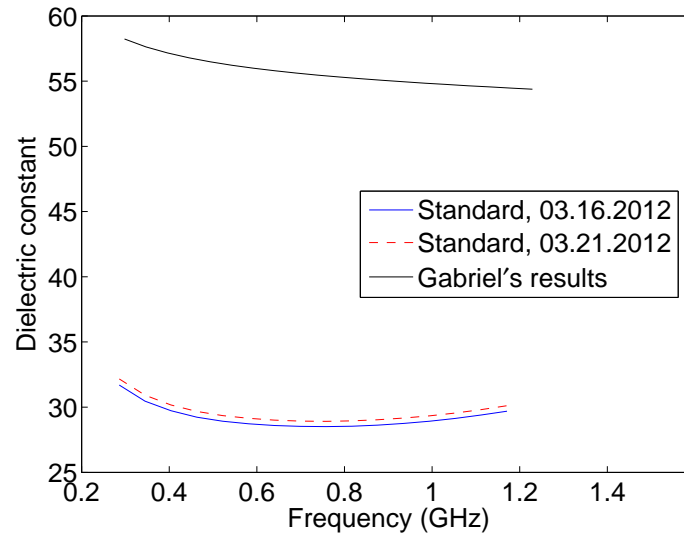


(a)

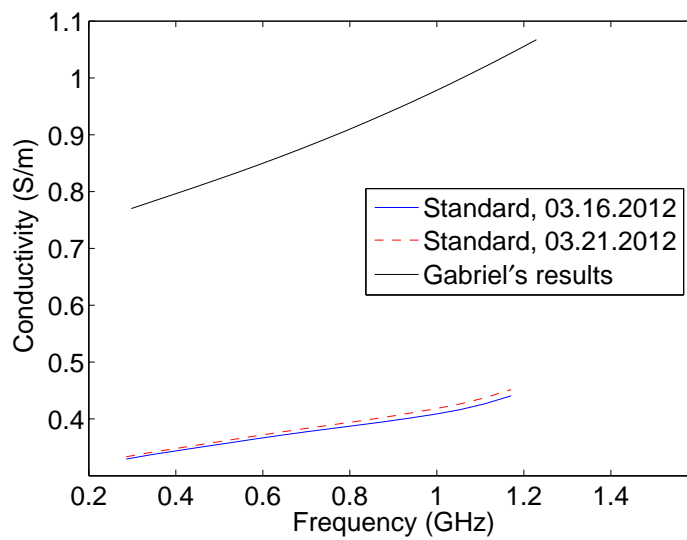


(b)

Figure 2.17: Results of measuring skin at NIST with Michael Janezic. Results are discussed on section 2.2.3.3



(a)



(b)

Figure 2.18: Results of measuring muscle phantom tissue at NIST with Michael Janezic. Results are discussed in section 2.2.3.3. Measurements are lower than expected.

Discussion of the results

Measurements did not lead to the expected results as were seen on Figures 2.17 and 2.18. Possible reasons for this error in measurements are:

- (1) The environment dries up the samples;
- (2) Procedure developed evaporates liquid, meaning the percentage of water on the mixtures is low;
- (3) Measurements of high permittivity materials carry a big error, underestimating the measured permittivity [14];
- (4) Imperfect contact between the sample and the probe leading to an underestimation of the measured permittivity, [51].

Mixtures are kept inside containers, but no humidifier is used. As Colorado's climate is dry, that could lead to a drying period between the mixing process and the measurements. Water is the main cause of high permittivity of the mixtures. Thus, a lack of water could decrease the value of the dielectric constant.

Secondly, the recipe taken from the literature [41] uses a complicated mixing device, which mixes everything in a perfectly sealed beaker where no vapor can escape. In our procedure, everything is boiled using an open beaker. When the mixture is heated up, steam is released, reducing the amount of water in the mixture and leading to a lower permittivity value.

Moreover, the reference used is Teflon with relative permittivity of 2.05 and very low conductivity. These values, compared to real tissue values, are very different, leading to a calibration process that may not be optimal for these measurements.

A final reason for these shifted measurements could be that the contact of the samples with the probe is not perfect, leading to underestimated measurements [14]. A sketch of this situation is shown in Figure 2.19.

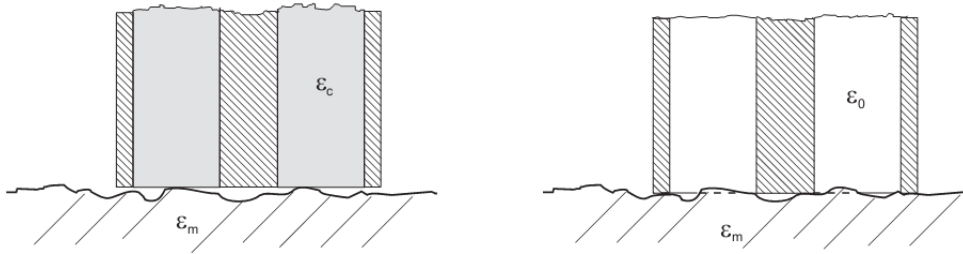


Figure 2.19: Contact between the probe and the sample surface. As the MUT is rough, the contact between the probe and the MUT might not be perfect, leading to an air gap. This air gap could be modeled as a capacitance which will decrease the values measured. Picture taken from [14].

Different mixtures were measured: high conductivity, low conductivity, high permittivity and standard. Standard mixtures are the same recipes presented in Section 2.1. High conductivity, low conductivity and high permittivity are mixtures that vary the amounts of components trying to see what they affect. Following the recipes shown above, and varying the amount of water, one may vary the dielectric constant value of the mixture, i.e. more water produces higher dielectric constant. Varying the amount of NaCl, one may vary the conductivity value, i.e. higher NaCl amount to higher conductivity. These two assumptions were made before measuring and the results correlate with them. In addition, it is interesting to notice that increasing the amount of water (high permittivity mixture) causes the conductivity to decrease. This is because the NaCl particles are diluted in more water hence decreasing the conductivity. On the other hand varying the amount of salt diluted also affects the permittivity values.

Finally, the standard mixtures were measured on different days and produced similar results. Assuming the mixing process is always the same, one may assure that the permittivity values of the mixtures are always the same and the process proposed is stable in different mixing conditions.

Chapter 3

Wearable antenna

Contents

3.1	Dipole antenna on tissue	53
3.1.1	Antenna design and performance	54
3.2	Patch antenna on tissue	58
3.2.1	Antenna design	59
3.2.2	Antenna performance	59
3.3	Effects of tissue antenna separation and tissue bending	60
3.3.1	Effects on the dipole	62
3.3.2	Effects on the patch antenna	66
3.4	Tissue variation effects on antenna performance	68

When antennas are used in contact with or very close to human tissues, new challenges and engineering problems appear. Applications where wearable antennas are used are listed in section 1.2. These applications are fairly new and most of the already mentioned challenges remain unsolved. Thus, it is important to understand the interaction between the antenna and the human tissues to solve these challenges. In the literature, e.g. [68], antennas performing in inhomogeneous media are discussed.

In this chapter, the interaction between antennas and tissues is studied. Half wavelength dipoles and patch antennas are used and extensively studied. Dipoles are used because they are one of the most studied and understood antennas. Patch antennas are studied because they have some interesting characteristics that make them good candidates for wearable applications. Deeper explanation may be found in section 3.2.

The final goal of the designs presented here is to be used for radiometry, giving some specific characteristics that radiometer may require. A radiometer is a device that captures black body radiation from matter and it is able to extract the temperature of the body from this received signal. Thus, antennas for radiometry applications require the following characteristics: (1) better interaction with the tissues than interaction with the surrounding environment; (2) narrow band operation because the radiometer will operate using long integration times; (3) frequency of operation under study, although first results show that the optimum frequency of operation is 1.41GHz, thus antennas presented here are designed to operate at this frequency; (4) small size in order to be wearable and comfortable; (5) the antenna has to allow some flexibility to be adapted to human body contour; and (6) the antenna will perform in a quite band, allocated for radio astronomy purposes, on the range between 1.4GHz and 1.427GHz, if the frequency is changed, this band should be changed as well.

In addition, when one tries to study wearable antennas used in radiometry applications, some principles in electromagnetics might be used: (1) reciprocity, considering that the power emitted by the antenna is the same as the power emitted by the tissues that the antenna will receive; and (2) the effective wavelength in a dielectric, which is the wavelength divided by the square root of the dielectric constant $\lambda_{eff} = \lambda_0/\sqrt{\epsilon_r}$. The first principle is very important to understand the studies carried out in this thesis. All the explanations below apply the power radiated by the antenna and its interaction with the tissues to model the power emitted by the tissues and received by the antenna.

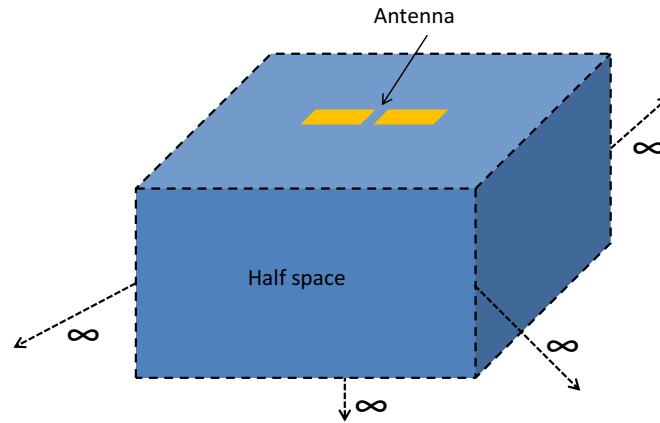
When modeling human tissues, many variations of problem characteristics appear: (1)

tissues' thickness variation; (2) layers' composition; (3) tissues' electrical properties; (4) fat index; etc. Hence, the following models are used to standardize all these possible variations:

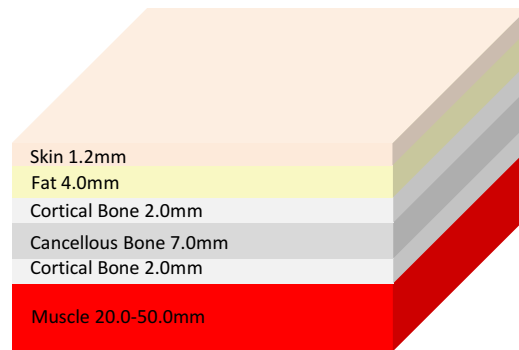
- (1) Half space: in order to simplify interaction between the antenna and the tissues, a model consisting of half free space-half tissue is used. The model is presented on figure 3.1(a). The model consists of filling an ideal infinite half space underneath the antenna with a phantom tissue with known electrical characteristics.
- (2) Layered stack of tissues: the model simulates human chest and consists of six layers of tissues: 1.2mm of skin [69], 4mm of fat [69], 2mm of cortical bone [70], 7mm of cancellous bone [70], a second layer (2mm) of cortical bone, and finally 20mm of muscle. Dielectric properties of the tissues are extracted from Gabriel's publication [28] and [38], which is the most widely accepted reference for dielectric constant and conductivity for biological tissues. The model is presented on figure 3.1(b).

When the presented designs are used in radiometry applications, the antenna performs in the near field because it is directly in contact with the tissues. Therefore, far field parameters are used only to characterize the antenna. Instead, reflection coefficient, input impedance, directivity and maximum electric field radiated are studied.

It is important to note that SAR (Specific Absorption Rate, [71]), or power absorbed by the tissues, is the parameter studied on the literature [72], [43] and [44] for radiometric applications along with the others already listed. SAR gives the most relevant information of how the power emitted by the antenna propagates through the tissues. If the final goal of the antenna design is to capture power emitted by the tissues, using the reciprocity principle, this is the main parameter that needs to be studied. Although SAR (or power absorbed) is the main parameter, the SAR measurements or simulations are not available due to problems with SEMCAD-X software and with the HFSS definition of SAR. Using the parameters listed on the previous chapter, a good idea of the antenna's performance and tissue-antenna interaction may be achieved.



(a)



(b)

Figure 3.1: Models used along with the antennas in order to study their performance in contact with dielectrics. On top the half space tissue model, where the antenna is placed on the top of the phantom. On the bottom, the layered model mimicking the human chest.

Antennas performing in the near field are usually called probes rather than antennas, in order to differentiate between near and far field applications.

3.1 Dipole antenna on tissue

Dipole antennas are probably the most widely used and studied antenna mainly due to their simplicity and very well known radiated fields. For this reason, dipole antennas are used to standardize or to understand the effects of tissues on antenna performance. Moreover, it is the easiest type of antenna to be compared in different situations already published and studied on the literature, e.g. [73, 74, 75].

The first step is to design the antenna under the optimum conditions to be used along with the tissue models presented before (Figure 3.1). The most commonly used dipole antenna is the half wavelength dipole. This type of antenna is particularly interesting to study because of its simple design and the very well known electromagnetic field components in free space:

$$E_{\theta} \simeq j\eta \frac{I_0 e^{-jkr}}{2\pi r} \left[\frac{\cos\left(\pi \cos\frac{\theta}{2}\right)}{\sin\theta} \right] \quad (3.1)$$

$$H_{\phi} \simeq j \frac{I_0 e^{-jkr}}{2\pi r} \left[\frac{\cos\left(\pi \cos\frac{\theta}{2}\right)}{\sin\theta} \right] \quad (3.2)$$

where r is the radial coordinate in the spherical coordinate system, θ and ϕ are the angle coordinates, I_0 is related to the current flowing into the dipole and η is the intrinsic impedance. In general, the length of the dipole is reduced to $l = 0.47\lambda$ so as to be easily matched to a typical transmission line, having its input impedance imaginary part canceled out. This gives the optimum frequency of operation as $f = c/\lambda$ where c is the speed of light in vacuum.

In this thesis, the optimum frequency of operation is defined as the frequency where the magnitude of the S_{11} parameter is minimized. This frequency is not always the same as the frequency where the imaginary part of the input impedance cancels out. The optimum

frequency of operation is defined as the lowest magnitude in S_{11} , because this is the situation where the antenna radiates the most power.

In Figure 3.2, a sketch of the dipole used in simulations is presented with the resonant frequency at 1.41 GHz.

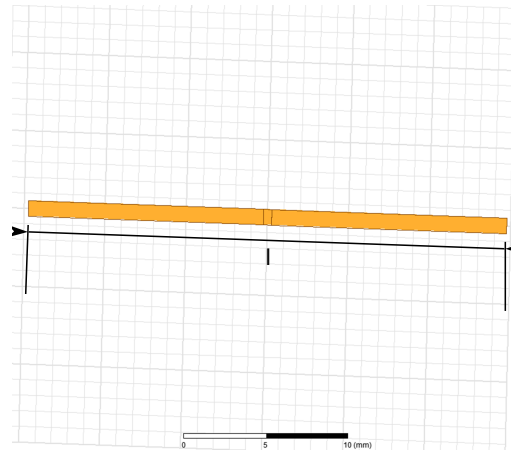


Figure 3.2: Sketch of dipole antenna used on simulations. Particularly, the antenna shown here, has a resonant frequency at 1.41GHz and a length of $l = 14.5mm$

3.1.1 Antenna design and performance

As mentioned previously, the antenna's length that determines the optimum frequency of operation is that where the magnitude of the reflection coefficient is minimized. In Figure 3.3, the optimization of the dipole's length is shown versus the frequency using the layered model shown in Figure 3.1(b). The same lengths are simulated in free space and compared to the lengths with tissues. Using these plots, one may define the effective dielectric constant as follows:

$$l_{no\ tissues} = l_{with\ tissues} \quad (3.3)$$

$$0.47\lambda_{no\ tissues} = 0.47\lambda_{with\ tissues} \quad (3.4)$$

$$\lambda_{0 \text{ no tissues}} = \frac{\lambda_{0 \text{ with tissues}}}{\sqrt{\epsilon_{eff}}} \quad (3.5)$$

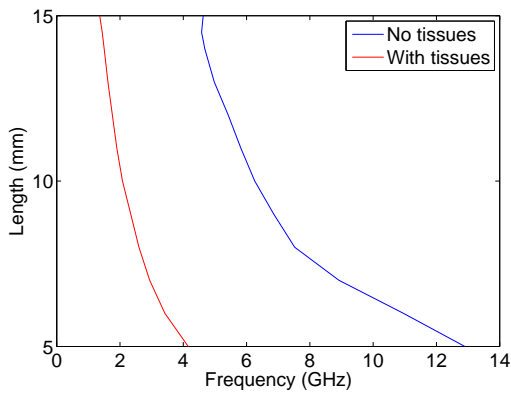
$$\frac{c}{f_{0 \text{ no tissues}}} = \frac{c}{f_{0 \text{ with tissues}} \sqrt{\epsilon_{eff}}} \quad (3.6)$$

and finally:

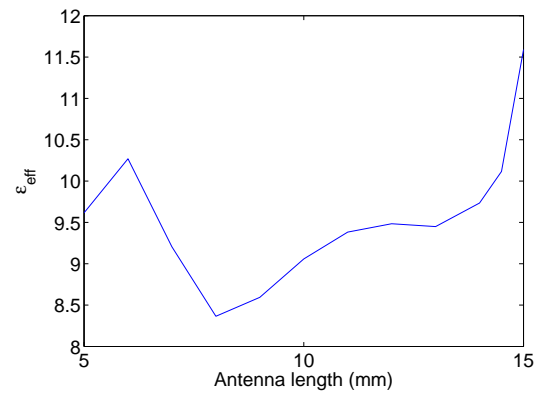
$$\epsilon_{eff} = \left(\frac{f_{0 \text{ no tissues}}}{f_{0 \text{ with tissues}}} \right)^2 \quad (3.7)$$

where ϵ_{eff} is the effective dielectric constant of the antenna operating with tissues. Using this relation, one may extract the effective dielectric constant from plot 3.3(b). As shown in the plot, the effective dielectric constant is around 10. The first tissue layer, skin, has a dielectric constant of 35 in this frequency range. This means that approximately the effective dielectric constant is about $1/4$ of the first layer (skin) dielectric constant ($\epsilon_r = 39.63$). However, it is likely that the other layers influence ϵ_{eff} to some extent as well.

In Figure 3.4(a) the magnitude of the S_{11} parameter is plotted versus frequency. In Figure 3.4(b) real and imaginary parts of the input impedance are plotted versus frequency. The antenna in contact with the tissues shifts its optimum frequency from 4.6GHz radiating into free space to 1.41GHz radiating in contact with tissues. In addition, the input reactance of the antenna with tissues has values between a few Ω and negative $j50\Omega$. The antenna's free space input reactance varies a lot more varying up to a few $k\Omega$. On the other hand, the real part in both cases is almost constant along the frequency range studied.

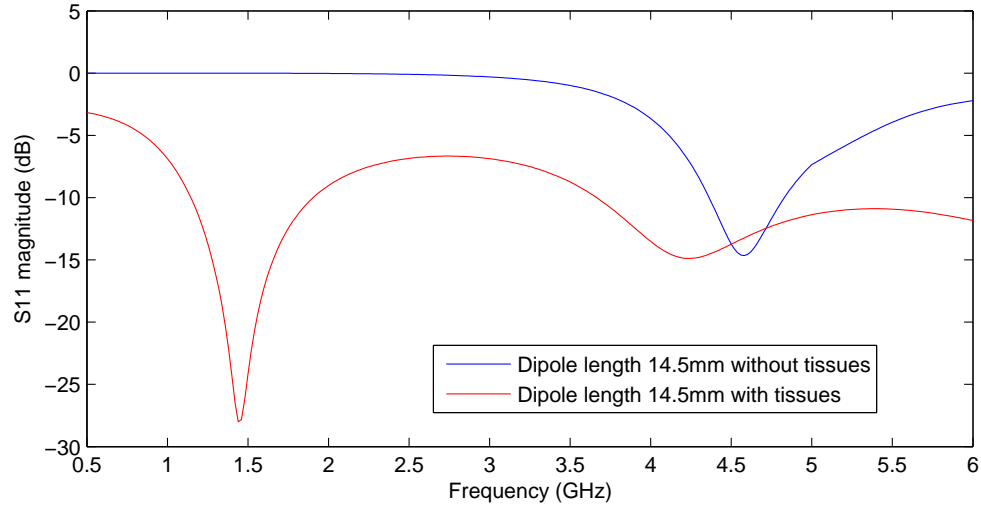


(a)

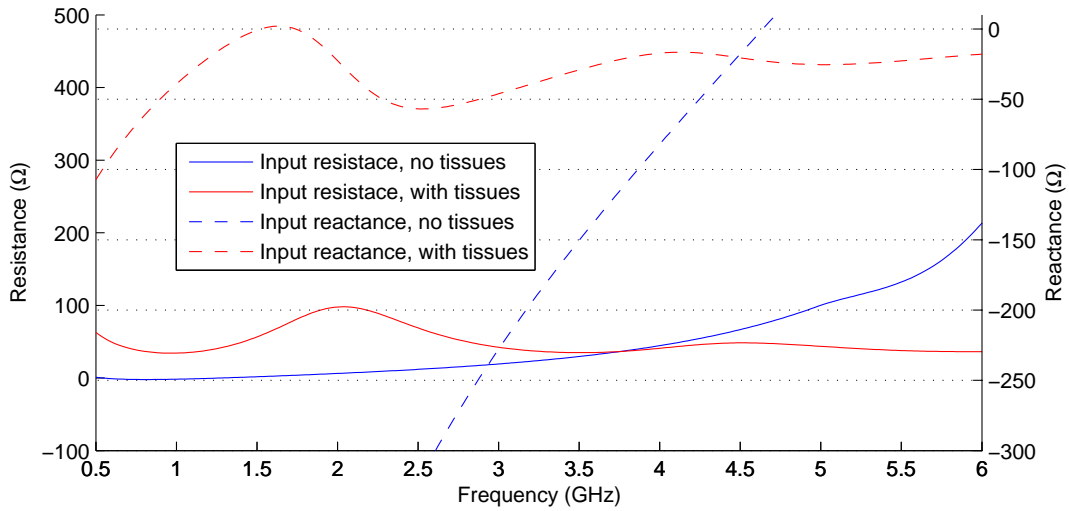


(b)

Figure 3.3: Optimization of dipole length on top of the stack of tissues shown in Figure 3.1(b). The left plot shows the relation between length and frequency. In red is the length of the dipole in contact with tissues and in blue the same length radiating on free space. In the right plot the effective dielectric constant was calculated from the previous relation.



(a)



(b)

Figure 3.4: Comparison of the resonant frequency between the antenna on top of the stack of tissues and radiating into free space. Figure 3.4(a) shows in red the S_{11} magnitude in dB of the dipole response radiating in contact with tissues; the same figure but in blue shows the S_{11} magnitude in dB of the antenna performing without the tissues, i.e. radiating into free space. Figure 3.4(b) shows the real (solid lines) and imaginary (dashed lines) parts of the input impedance of the antenna with (in red) and without the tissues (in blue). Figure 3.4(a) is normalized to a 50Ω characteristic impedance line.

3.2 Patch antenna on tissue

A design of a patch antenna is presented. This design is suitable to be used along with radiometry applications due to its characteristics explained below. Dimensions of the final design with the ground plane are 58x114mm. Hence, a miniaturization process may follow in future work.

Some reasons are behind choosing this type of antenna:

- (1) Very well known radiation characteristics that can be compared with published results;
- (2) A ground plane is incorporated on the antenna's design, increasing the antenna's directivity into the tissues and shielding the antenna from the surrounding environment;
- (3) Possibility of miniaturization of the antenna's dimensions;
- (4) Narrow band, avoiding the possibility of capturing radiation from undesired bands.

The radiometer will work with long integration times, allowing narrow band captures instead of broadband and short integration times.

The characteristics of the patch antenna perfectly fit the requirements listed above, making the antenna a perfect candidate to be used as a probe for the radiometer device.

In general, patch antennas require a thick substrate whose dielectric constant is low for a good performance, better efficiency, larger bandwidth but a larger surface area is then required. On the other hand, a higher dielectric constant of the substrate leads to smaller radiating surfaces and smaller dimensions. Wearable antennas for radio thermometers require flexibility, narrow band and small size. Performance in the far-field is not considered critical. For this reason, a mid dielectric constant substrate ($\epsilon = 6.15$) and thin substrate (25 mil) are chosen.

3.2.1 Antenna design

A sketch of the proposed antenna is shown in Figure 3.5. The antenna is a rectangular patch with radiating surface dimensions of $L=40.2\text{mm}$ and $W=22\text{mm}$. The feed is via coaxial line through the ground plane and it has an 8mm offset along the L axis. The feed contact with the radiating surface is modeled as a point. The contact with the ground plane is modeled as the contact point between the outer conductor of the coaxial line and the ground. A flexible substrate is used for further studies on antenna bending. The substrate used is Rogers/duroid 6006 [76] with a dielectric constant of 6.15 and a dissipation factor of 0.0027. The substrate's thickness is 25 mil, which was chosen because it allows for some flexibility, which is important if the antenna has to be shaped according to the human body, as mentioned. The dimensions of the antenna are chosen using optimization tools available on electromagnetic commercial software, as closed form equations and methods for the antenna's design may not apply. The reason why normal patch antenna design equations cannot be used, is because the antenna is in contact with a stack of tissues. There are some publications that show the antenna's performance in contact with dielectrics [77], [78] and [79]. The scenario used in this thesis is rather unique and a full parametric analysis has to be performed after an initial design using the equations presented in these publications. The antenna being designed is placed over a layered model of the human chest shown in Figure 3.1(b) and Figure 3.8(a).

3.2.2 Antenna performance

A comparison between the radiation characteristics into free space and in contact with the tissues is shown in Figure 3.6.

Figure 3.6 shows the antenna's performance radiating in contact with tissues and into free space. This antenna is narrow band, having a -10dB bandwidth of 16MHz and an operating frequency of 1.395GHz when operated in contact with the tissues as shown in Figure

3.6(a). In addition, when the antenna radiates into free space, two operation frequencies appear at 1.48GHz and 2.87GHz as shown in the same figure. Figure 3.6(b) shows the real and imaginary parts of input impedance versus frequency. The real part shows peaks at the operating frequencies, allowing the antenna to radiate. Reactance shows peaks at the operating frequencies, thus they are also resonant frequencies.

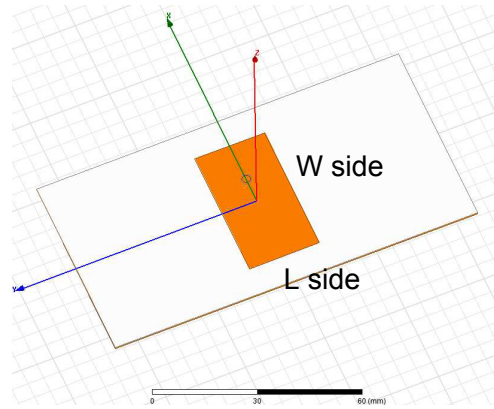
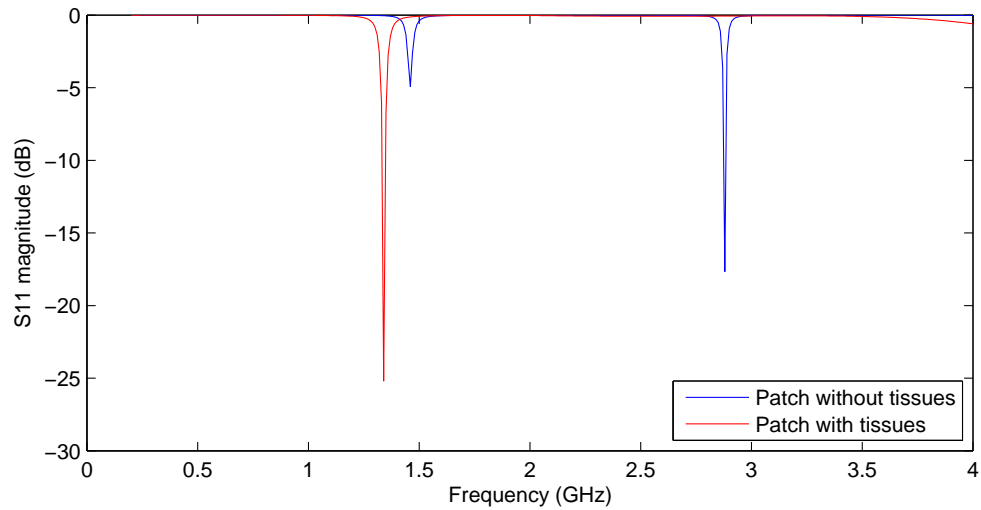


Figure 3.5: Drawing of the antenna design in free-space. It is important to note the ground plane shape being narrower in the radiation side of the antenna (L side).

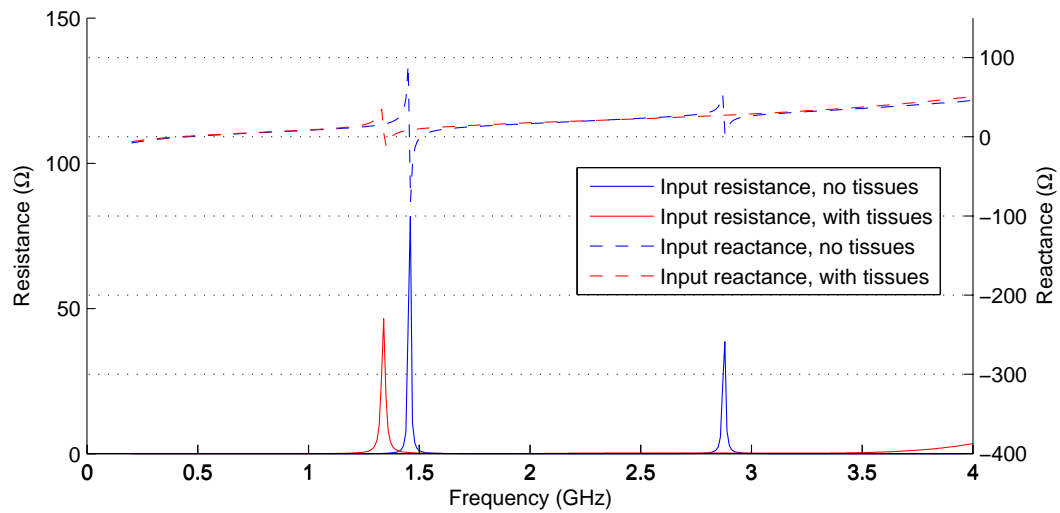
3.3 Effects of tissue antenna separation and tissue bending

Full-wave simulations are conducted through different models in order to study antenna performance and effects on the field's propagation in different scenarios. These scenarios model real situations where the antenna will not have perfect contact with the tissues. In order to cover the most realistic scenarios, four studies are conducted:

- (1) Antenna radiation in free space (explained before);
- (2) Antenna with perfect contact with tissues (explained before);



(a)



(b)

Figure 3.6: Comparison of the antenna's performance in free space and in contact with tissues, in blue and red respectively in both figures. Figure 3.6(a) plots the magnitude of the S_{11} parameter. Figure 3.6(b) shows imaginary (dashed lines) and real (solid lines) parts of the input impedance. Figure 3.6(a) is normalized to a 50Ω characteristic impedance line.

(3) Separation between the antenna and the tissues:

- (a) Planar separation: Figures 3.7(b) and 3.8(b), where the antenna and the tissues are separated while keeping the two parallel, i.e. perpendicular separation;
- (b) One side bending Figures 3.7(c) and 3.8(c), where tissues are bent only on one side;
- (c) Two sides bending Figures 3.7(d) and 3.8(d), where tissues are bent on both sides;

Two different antennas are studied, the half-wavelength dipole (Figure 3.7) and the patch (Figure 3.8).

3.3.1 Effects on the dipole

In Figure 3.9(a), the bending and the separation of the tissues versus the frequency of operation of the dipole is plotted. Increasing the bending of the tissues or the separation, increases the optimum frequency of operation shifting it towards the frequency of the free space case. Bending the two sides has the least effect on the antenna's performance, while perpendicular separation has the biggest effect. After separating the tissues a few tenths of a millimeter, the frequency shifted 0.5GHz, making the antenna no longer suitable to work at the desired frequency. In Figure 3.9(b), the bending and the separation of the tissues versus the magnitude of the reflection coefficient at the frequency of operation of the dipole is plotted. It can be seen that the tissue bending affects the magnitude of the reflection coefficient considerably, making its magnitude decrease rapidly. If the separation is more than 0.25mm, the magnitude of the reflection coefficient increases above -10dB and the antenna becomes no longer useful.

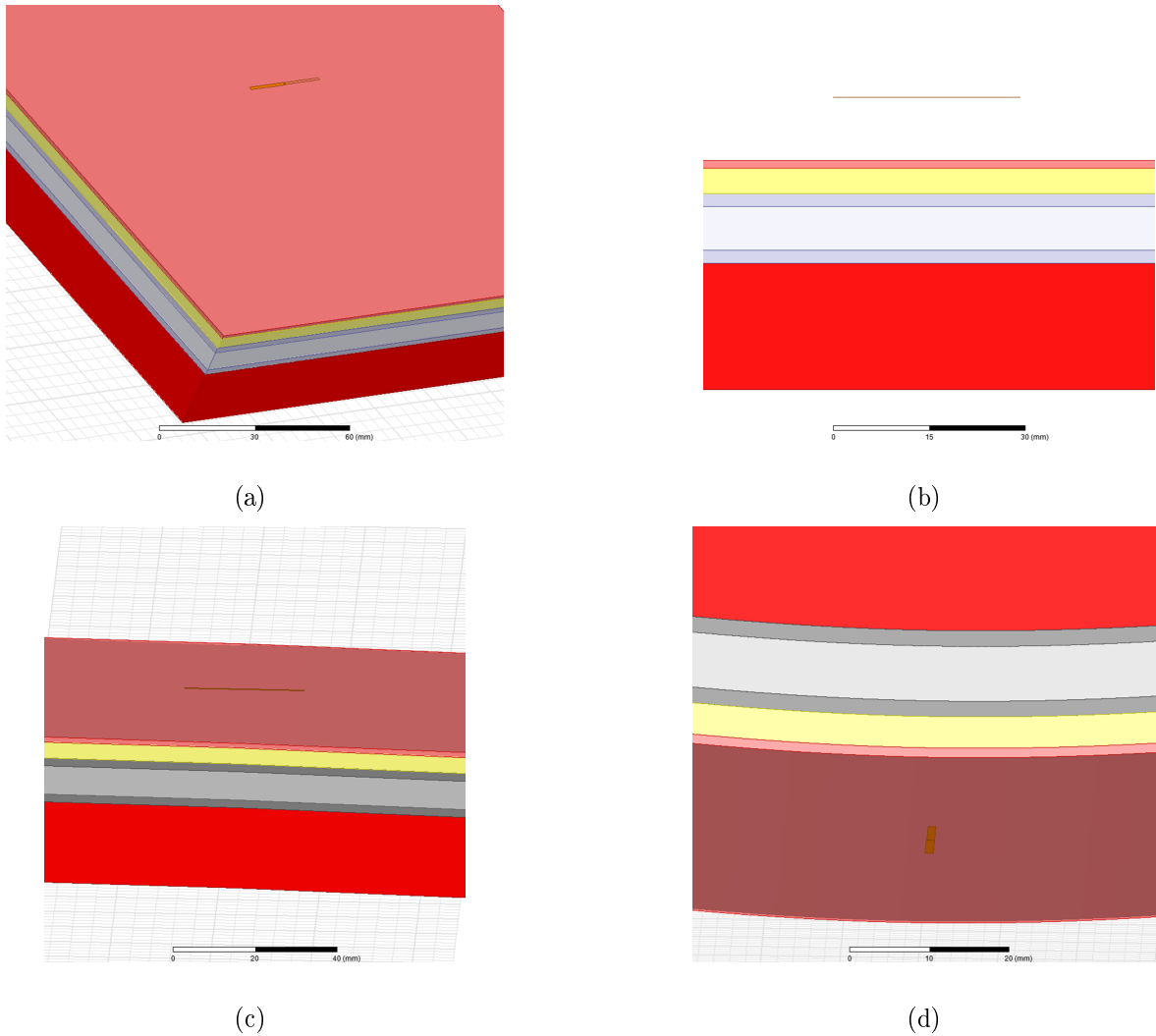


Figure 3.7: Sketch of the different scenarios studied with the dipole antenna. 3.7(a) shows the dipole on top of the stack of tissues; 3.7(b) shows the dipole on top of the stack of tissues having a perpendicular separation between the tissues and the antenna; 3.7(c) shows the dipole on top of the stack of tissues with one side separation; and 3.7(d) shows the dipole on top of the stack of tissues with both sides separation.

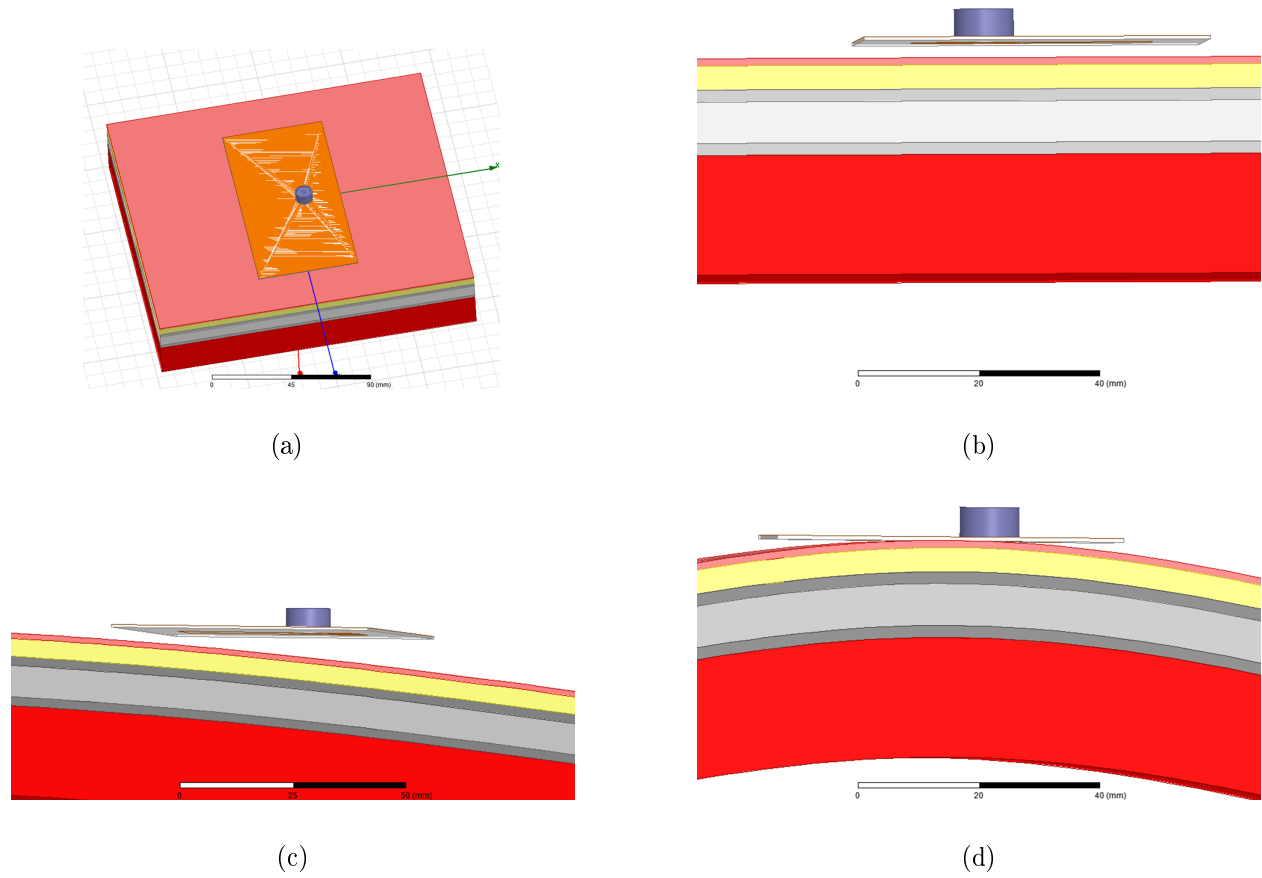


Figure 3.8: Sketch of the different scenarios studied with the patch antenna. 3.8(a) shows the patch on top of the stack of tissues; 3.8(b) shows the patch on top of the stack of tissues having perpendicular separation between the tissues and the antenna; 3.8(c) shows the patch on top of the stack of tissues with one side separation; and 3.8(d) shows the patch on top of the stack of tissues with both sides separation.

In Figure 3.10, how the bending affects the input impedance of the antenna is shown. The bending is plotted versus the resistance and the reactance of the antenna. Results show a decrease of the resistance and an increment towards negative values of the reactance leading the antenna towards a purely imaginary input impedance. Thus, the antenna will not radiate when separated from the tissues.

The most interesting point of these plots is how the antenna is more sensitive to one side separation than two side separation.

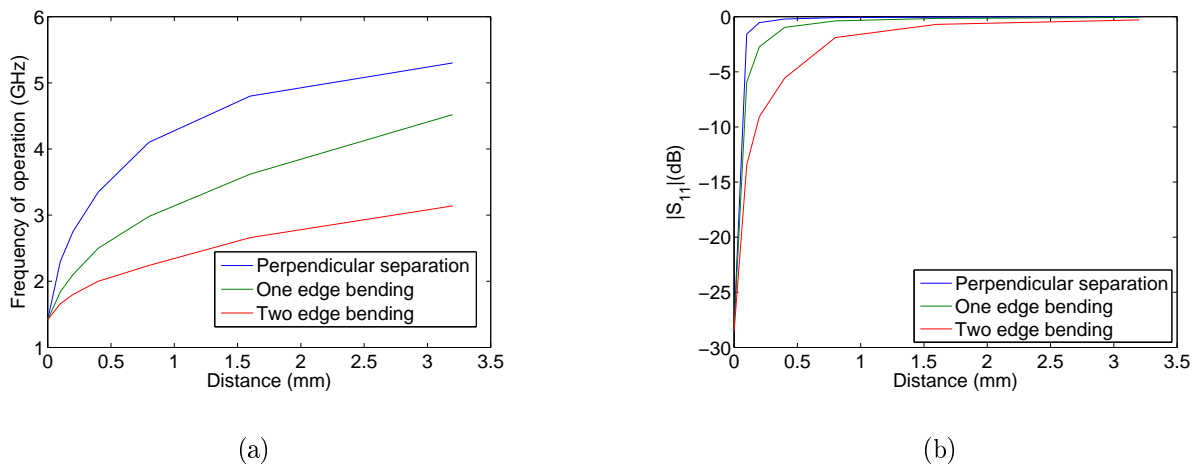


Figure 3.9: Frequency of operation of the dipole performing in the different scenarios described before in Figure 3.7. Figure 3.9(a) shows the optimum frequency of operation. Figure 3.9(b) shows the magnitude of the reflection coefficient at the operating frequency (1.41GHz). The figures show in red the effects of one side bending , in green the effects of two sides bending and in blue the perpendicular separation effects.

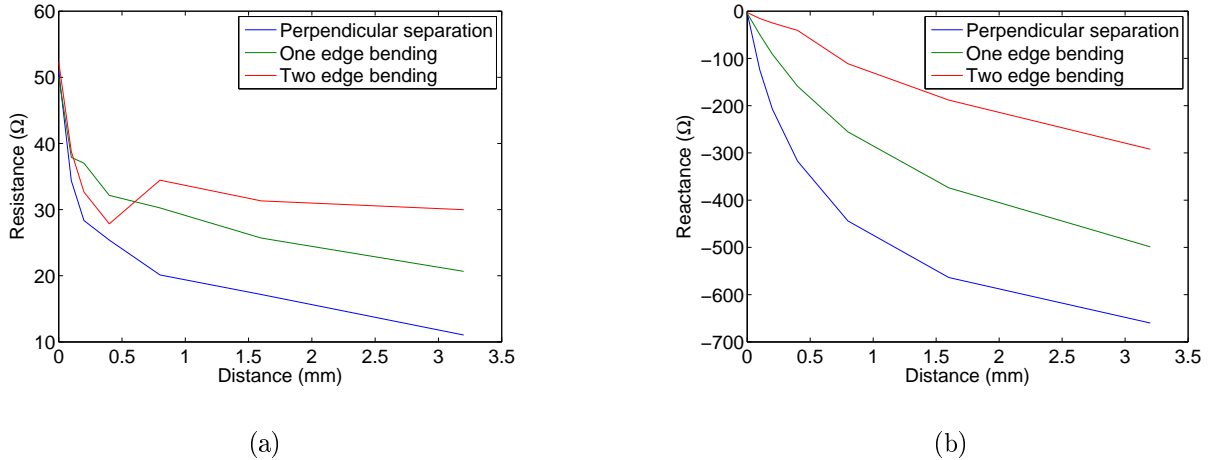


Figure 3.10: The plot shows how the bending of the tissues affect the input impedance of the dipole. Figure 3.10(a) plots the input resistance and Figure 3.10(b) shows the input reactance. The figures show in red the effects of one side bending, in green the effects of two sides bending and in blue the perpendicular separation effects.

3.3.2 Effects on the patch antenna

In Figure 3.11(a) the bending and separation of the tissues versus the optimum frequency of operation of the dipole are plotted. Increasing the bending of the tissues or the separation, increases the optimum frequency of operation shifting towards the frequency of the free space. Two side bending has the least effect on the antenna's performance, while perpendicular separation has the biggest effect. After separating a few tenths of a millimeter, the frequency shifted 0.5GHz making the antenna not longer suitable to work at the desired frequency. In Figure 3.11(b), the bending and separation of the tissues versus the magnitude of the reflection coefficient at the frequency of operation of the dipole is plotted. It can be seen, that the tissue's bending affects the magnitude of the reflection coefficient considerably making its magnitude increase rapidly. If the separation is more than 0.25mm the magnitude of the reflection coefficient increases above -10dB and the antenna becomes no longer useful.

In Figure 3.12, how the bending affects the input impedance of the patch antenna

is shown. The bending is plotted versus the resistance and the reactance of the antenna. Results show a decrease of the resistance and an increment towards positive values of the reactance leading the antenna to a purely imaginary input impedance. Thus, the antenna will not radiate when separated from the tissues. It is interesting to note the peak of the input reactance when the separation of the tissues is very small.

The patch antenna is especially interesting to study because the radiation through the edges is not uniform. In a patch antenna, most of the electric field is confined to the L side. Plots just mentioned show that the antenna performance is more sensitive to the bending or separation effects of the tissue along the L side than to the effect of bending or separating them along W side. Moreover, plots show how the antenna is more sensitive to one side separation than both sides separation.

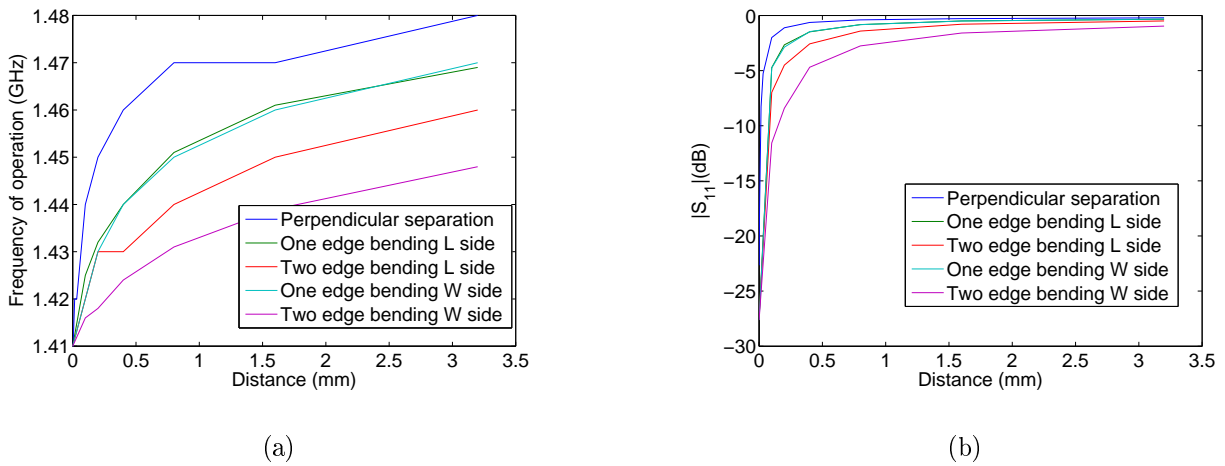


Figure 3.11: Performance of the patch in the different scenarios described before. Figure 3.11(a) shows the optimum frequency of operation. Figure 3.11(b) shows the magnitude of the reflection coefficient at the operating frequency. Figures show in blue the perpendicular separation between the antenna and the dipole; in green the one edge bending, being L side dark green and W side light green; in purple the two edge bending along W side and in red the two edges bending along L side.

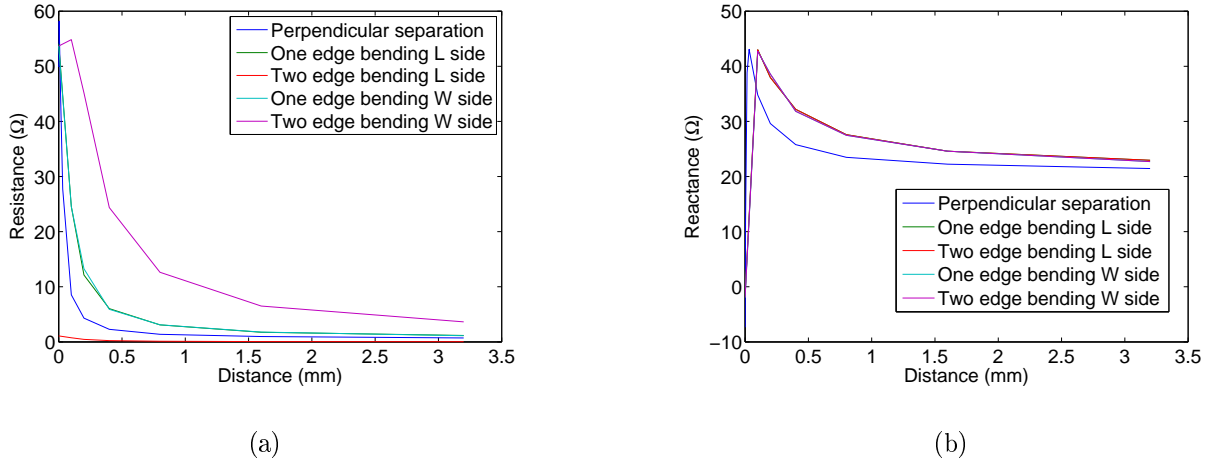


Figure 3.12: These plots show how the bending of the tissues affect the input impedance of the patch. Figure 3.12(a) shows the input resistance and Figure 3.12(b) shows the input reactance of the patch antenna. Figures show in blue the perpendicular separation between the antenna and the dipole; in green the one edge bending, being L side dark green and W side light green; in purple the both edges bending along W side and in red both edges bending along L side.

3.4 Tissue variation effects on antenna performance

Along with the studies presented previously, it is interesting to study how variations in the conductivity and dielectric constant may affect the antenna's performance. Figure 3.13 shows how different tissues affect the length of the dipole. The optimum length of the dipole shows that the variation of the tissues properties does not affect the antenna's performance in a consistent way. Thus, it is very interesting to study the tissue properties variation and its effects on antenna performance.

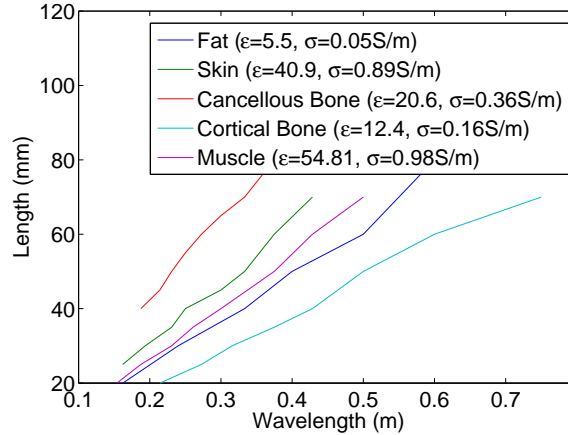


Figure 3.13: The figure shows the optimum length of the dipole in contact with the different tissues. The model used is the half space phantom, shown in Figure 3.1(a).

In this section the dipole antenna presented before is studied with the tissues stack model (Figure 3.1(b)). The dielectric constant and the conductivity of the phantom layers is varied from the standard value presented in Gabriel's publications [28, 38, 39]. The relative variation of the dielectric constant and conductivity is shown.

Figure 3.14(a) shows the optimum frequency of operation of the dipole with the stack of tissues varying the tissues dielectric constant. The optimum frequency of operation increases when the relative dielectric constant of any tissue decreases, while the optimum frequency of operation decreases when the dielectric constant of the tissues increases. These are the results expected because the length of the dipole is inversely proportional to the dielectric constant (or effective dielectric constant as defined in Equation 3.6). Thus, when the dielectric constant decreases the frequency has to increase and vice versa.

Figure 3.14(b) shows the magnitude of the reflection coefficient of the dipole with the stack of tissues varying the tissues dielectric constant. The magnitude of the reflection coefficient has its minimum in the designed frequency range and increases when the tissues' dielectric constant increases for the two most superficial layers. It can be seen also that the effects of the muscle dielectric constant variation are important although the muscle is the

deepest layer. Moreover, the cancellous bone affects the results as well but only for variation of the dielectric constant to higher values.

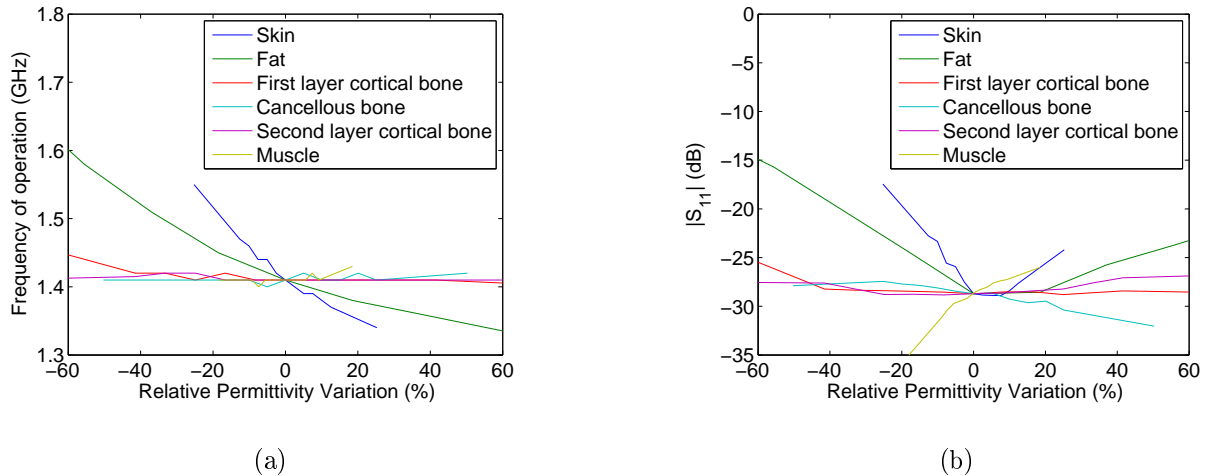


Figure 3.14: Figure 3.14(a) shows the variation of the optimum frequency of operation of the dipole due to variations in the dielectric constant of the tissues. Figure 3.14(b) shows the variation the magnitude of the reflection coefficient of the dipole at the designed frequency (1.41GHz) due to tissue dielectric constant variations. Figures show the conductivity variation of the skin in blue, of the fat in green, of the first layer of cortical bone in red, of the cancellous bone in cyan, of the second layer of cortical bone in magenta and of the muscle in yellow.

Figure 3.15(a) shows the input resistance of the dipole above the stack of tissues (Figure 3.1(b)) while the dielectric constant of the tissues is being varied. Figure 3.15(b) shows the input reactance of the dipole above the stack of tissues while the dielectric constant of the tissues is being varied. In all the cases, the input resistance and reactance decrease when the dielectric constant decreases and vice versa.

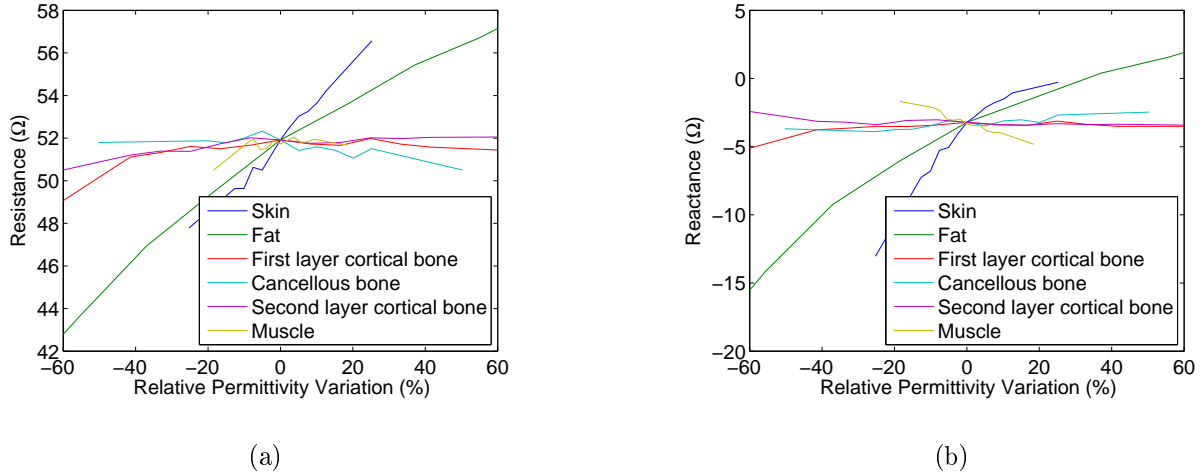


Figure 3.15: Figure 3.15(a) shows the variation of the input resistance of the dipole at the designed frequency (1.41GHz) due to variations in the dielectric constant of the tissues. Figure 3.15(b) shows the variation of input reactance of the dipole at the designed frequency (1.41GHz) due to variations in the dielectric constant of the tissues. Figures show the conductivity variation of the skin in blue, of the fat in green, of the first layer of cortical bone in red, of the cancellous bone in cyan, of the second layer of cortical bone in magenta and of the muscle in yellow.

Figure 3.16(a) shows the optimum frequency of operation of the dipole with the stack of tissues while their conductivity is varied. Similarly to the dielectric constant effects, when the conductivity of the tissues increases, the optimum frequency of operation decreases and vice versa. Especial mention to the muscle effects that affects in differently increasing the antenna's optimum frequency of operation when its conductivity increases and vice versa.

Figure 3.16 shows the magnitude of the reflection coefficient of the dipole with the stack of tissues while their conductivity is varied. The magnitude of the reflection coefficient peaks when the conductivity of the tissues varies. This effect might be expected as the antenna is designed to operate in the scenario with no variation, thus when we vary the conductivity mainly leads to an increment on the reflection coefficient value.

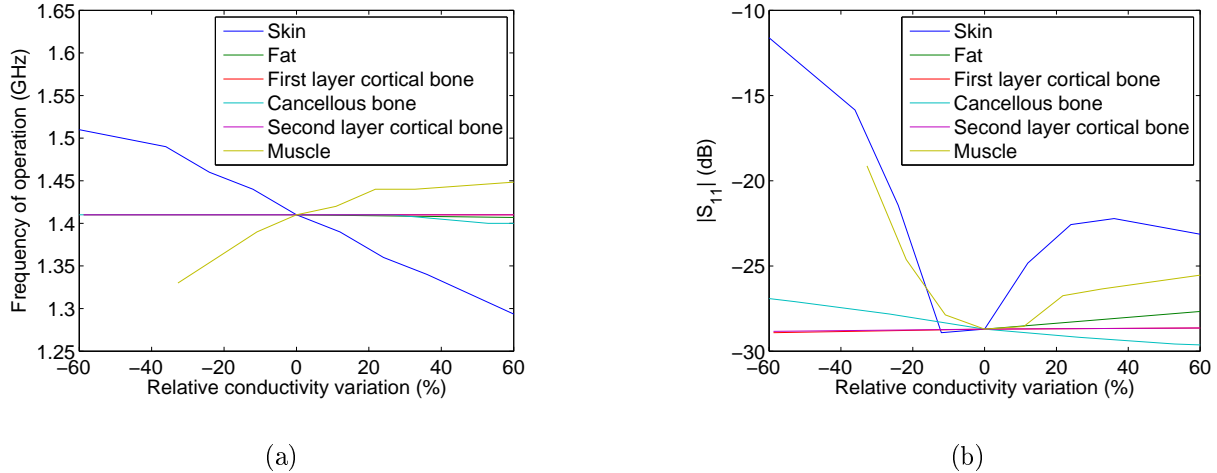
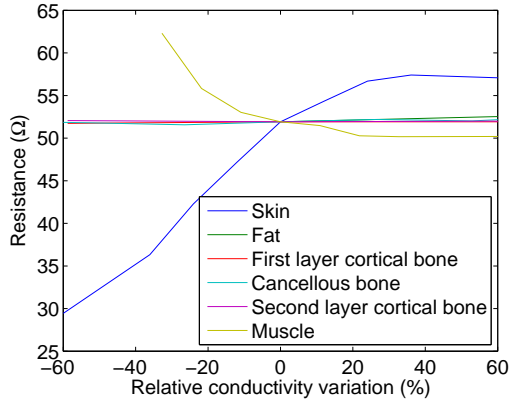
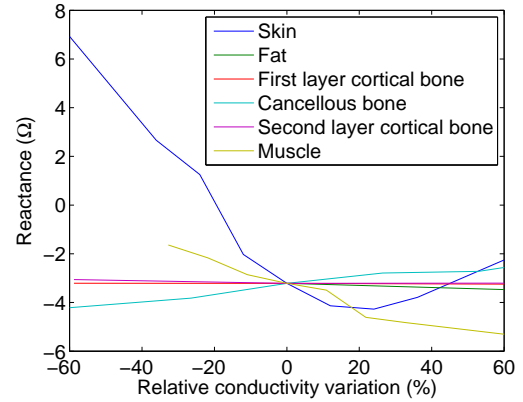


Figure 3.16: Figure 3.16(a) shows the variation of the optimum frequency of operation of the dipole due to variations in the conductivity of the tissues. Figure 3.16(b) shows the variation of the reflection coefficient magnitude of the dipole at the designed frequency (1.41GHz) due to variations in the conductivity of the tissues. Figures show the conductivity variation of the skin in blue, of the fat in green, of the first layer of cortical bone in red, of the cancellous bone in cyan, of the second layer of cortical bone in magenta and of the muscle in yellow.

Figure 3.17(a) shows variation of the input resistance of the dipole with the stack of tissues while the tissues conductivity is varied. Figure 3.17(b) shows the input reactance of the dipole with the stack of tissues while the tissues conductivity is varied. The effects on the input resistance are close to dielectric constant effects, increasing input resistance with the increment of the conductivity and vice versa. Note the decreasing of the input resistance after the increment of the skin's conductivity. Note also the more dependence of the input resistance on the fat's conductivity variation which increases the input resistance significantly. Moreover, note the effects of the muscle's conductivity variation to lower values which increases the input resistance. On the other hand, the input reactance has a minimum peak for skin and fat variation at a slightly higher conductivity value. The two kinds of bones increase the value of the input reactance or it keeps almost constant. Finally again, notice the effects of the muscle's conductivity increment which decreases the input reactance.



(a)



(b)

Figure 3.17: Figure 3.17(a) shows the variation of input resistance of the dipole at the designed frequency (1.41GHz) due to tissue variations in the conductivity of the tissues. Figure 3.17(b) shows the variation of input reactance of the dipole at the designed frequency (1.41GHz) due to tissue conductivity variation. Figures show the conductivity variation of the skin in blue, of the fat in green, of the first layer of cortical bone in red, of the cancellous bone in cyan, of the second layer of cortical bone in magenta and of the muscle in yellow.

Chapter 4

Conclusions and future work

Contents

4.1	Summary	75
4.2	Future work	76
4.3	Conclusions	77

In summary, an extensive study of antennas performing in contact with tissues and phantom tissues making process are presented.

The antenna design in the presence of tissues is focused on the microwave thermometry application. Here an antenna placed in the near field of a body is used to detect noise power radiated from different tissues inside the body. This antenna might be used in several applications already listed in previous sections, but its intended use is for thermo-radiometric applications.

Currently, there are no commercial technologies for internal body temperature measurements. Internal body temperature can be estimated from several external measurements, but this method is not reliable. Another approach used in the military for monitoring overheating of soldiers under heavy training or in hot climates, is a wireless pill thermometer which remains in the body for an unknown length of time and only measures the temperature of the intestine [25]. Furthermore, there are different methods that are very invasive and

extremely uncomfortable for patients, methods such as rectal temperature measurements, which use a normal mercury thermometer or a special probe; and esophageal temperature measurements, which use a thermistor inserted through the nasal passages which can cause irritation. A common method is the use of infrared (IR) thermometers, which only measures surface temperature and are usually tympanic, i.e. inserted in the ear [26]. Thus, microwave radio thermometry is a method with a huge range of applications.

In the following sections conclusions of this work are presented. In addition, future work related to unresolved issues regarding this thesis are presented.

4.1 Summary

There are two main conclusions of this work. The first one is the development of phantom tissues that mimic electric properties of tissues and are used to validate wearable antenna designs. The second conclusion of this work is the extensive study of wearable antennas performed and the results already presented.

Along with these two conclusions, more specific statements may be made:

- (1) Phantom tissues:
 - (a) Experimental mixtures had discrepancies with expected results by a factor of 2
 - (b) Improvements of mixture recipes is necessary. Mixtures for mimicking other human tissues, e.g. bones are also needed.
- (2) Complex permittivity measurements:
 - (a) A new technique is proposed and studied based on inhomogeneous microstrip lines. Some publications using similar methods have recently been published demonstrating that this is still an issue of controversy, e.g. [80].
 - (b) Two other techniques were also studied (free-space and coaxial probe) and compared

- (3) Wearable antenna design:
 - (a) Dipole and patch antennas designed on layered tissue using full-wave EM simulations
 - (b) Dipole and patch compared for different applications
- (4) Interaction between antennas and tissues:
 - (a) Imperfections expected in a real application were studied numerically, e.g. tissue bending
 - (b) Better understanding of effects of tissues on the far field in air and in tissue
- (5) Simulation towards design:
 - (a) Full-wave electromagnetic CAD tools must be used carefully when designing wearable antennas
 - (b) Wearable antennas interact with the human body in the near field
 - (c) Simulations take a lot of computing resources, so simplifications based on physical understanding are useful

4.2 Future work

Given the encouraging results from this preliminary study, it is straightforward to outline plans for future work in this area:

- (1) Improve techniques to mix phantom tissues to enable models that perfectly mimic human tissues in the specified frequency range. This will require another mixing and validating effort. The results will be the perfect tool to validate wearable antenna designs in any microwave research laboratory.

- (2) Perform a more detailed analysis of the permittivity measurement technique based on microstrip fixtures, looking carefully to the problems already listed.
- (3) Perform miniaturization of the patch antenna design presented on previous sections, resulting in a very good candidate for radiometry applications.
- (4) Study of different antenna designs. Perform multiple wearable antenna designs to cover frequency bands that are not studied in this thesis. One may want to take a look to the literature, e.g. [81].
- (5) Numerical and experimental studies of the effect of position and other variables, such as the tissues' thickness, on different parts of the body need to be performed.
- (6) Study the power absorbed by the tissues and its interaction with the other tissues and the antenna.
- (7) Multi-band antennas may be studied in order to have different penetration depths in order to interrogate tissues in different positions of the body.
- (8) Once phantom tissue models are improved, combine these with antenna designs and validate simulations

4.3 Conclusions

The results confirmed the choices made through the learning process. In addition, some future work must be done to finally conclude open issues.

Even though the first approach to the topic was difficult to define, at the end we may conclude that the learning process and the studies performed achieved very promising results.

Throughout the work performed in this thesis, I was able to apply electrical engineering knowledge acquired during my previous education on the always challenging field of biology. Along with all the studies presented, I was able to learn about biology and the engineering

point of view of biological systems. Scientific discussions derived from my work and personal experiences are remarkable conclusions of this work.

Bibliography

- [1] J. Van der Zee, "Heating the patient: a promising approach?" *Annals of Oncology*, vol. 13, no. 8, pp. 1173–1184, 2002, 10.1093/annonc/mdf280.
- [2] G. A. Ybarra, L. Qing Huo, J. P. Stang, and W. T. Joines, "Microwave breast imaging," *American Scientific Publishers*, 2007.
- [3] S. Ullah, H. Higgins, B. Braem, B. Latre, C. Blondia, I. Moerman, S. Saleem, Z. Rahman, and K. Kwak, "A comprehensive survey of wireless body area networks," *Journal of Medical Systems*, pp. 1–30, 2010.
- [4] F. Merli, L. Bolomey, E. Meurville, and A. K. Skrivervik, "Implanted antenna for biomedical applications," in *Antennas and Propagation Society International Symposium, 2008. AP-S 2008. IEEE*, pp. 1–4.
- [5] U. Kaatze, "Complex permittivity of water as a function of frequency and temperature," *Journal of Chemical and Engineering Data*, vol. 34, no. 4, pp. 371–374, 1989.
- [6] D. Miklavcic, N. Pavselj, and F. X. Hart, "Electric properties of tissues," *Wiley Encyclopedia of Biomedical Engineering*, 2006.
- [7] D.-H. Kim, N. Lu, R. Ma, Y.-S. Kim, R.-H. Kim, S. Wang, J. Wu, S. M. Won, H. Tao, A. Islam, K. J. Yu, T.-i. Kim, R. Chowdhury, M. Ying, L. Xu, M. Li, H.-J. Chung, H. Keum, M. McCormick, P. Liu, Y.-W. Zhang, F. G. Omenetto, Y. Huang, T. Coleman,

- and J. A. Rogers, "Epidermal electronics," *Science*, vol. 333, no. 6044, pp. 838–843, 2011, 10.1126/science.1206157.
- [8] L. Gil-Young, D. Psychoudakis, C. Chi-Chih, and J. L. Volakis, "Omnidirectional vest-mounted body-worn antenna system for UHF operation," *Antennas and Wireless Propagation Letters, IEEE*, vol. 10, pp. 581–583, 2011.
- [9] Mobipedia, "Wearable antennas for military smartphones," 2012.
- [10] O. Sotoudeh and T. Witting, "Electromagnetic simulation of mobile phone antenna performance," *Microwave Journal*, 2007.
- [11] F. Jaspard and M. Nadi, "Dielectric properties of blood: an investigation of temperature dependence," *Physiological Measurement*, vol. 23, no. 3, p. 547, 2002.
- [12] S. S. Stuchly, C. L. Sibbald, and J. M. Anderson, "A new aperture admittance model for open-ended waveguides," *Microwave Theory and Techniques, IEEE Transactions on*, vol. 42, no. 2, pp. 192–198, 1994.
- [13] Z. X. Shen and R. H. MacPhie, "A simple method for calculating the reflection coefficient of open-ended waveguides," *Microwave Theory and Techniques, IEEE Transactions on*, vol. 45, no. 4, pp. 546–548, 1997.
- [14] R. Olmi, M. Bini, A. Ignesti, and C. Riminesi, "Non-destructive permittivity measurement of solid materials," *Measurement Science and Technology*, vol. 11, no. 11, p. 1623, 2000.
- [15] J. R. Mosig, J. C. E. Besson, M. Gexfabry, and F. E. Gardiol, "Reflection of an open-ended coaxial line and application to non-destructive measurement of materials," *IEEE Transactions on Instrumentation and Measurement*, vol. 30, no. 1, pp. 46–51, 1981.
- [16] J. P. Grant, R. N. Clarke, G. T. Symm, and N. M. Spyrou, "A critical study of the open-ended coaxial line sensor technique for RF and microwave complex permittivity

- measurements,” *Journal of Physics E: Scientific Instruments*, vol. 22, no. 9, p. 757, 1989.
- [17] A. M. El-Sharkawy, P. P. Sotiriadis, P. A. Bottomley, and E. Atalar, “A new RF radiometer for absolute noninvasive temperature sensing in biomedical applications,” in *Circuits and Systems, 2007. ISCAS 2007. IEEE International Symposium on*, pp. 329–332.
- [18] E. C. Fear, S. C. Hagness, P. M. Meaney, M. Okoniewski, and M. A. Stuchly, “Enhancing breast tumor detection with near-field imaging,” *Microwave Magazine, IEEE*, vol. 3, no. 1, pp. 48–56, 2002.
- [19] C. H. Jones and D. M. Whitaker, “A numerical reference marker for the rank thermographic system,” *British Journal of Radiology*, vol. 45, no. 532, pp. 311–313, 1972, 10.1259/0007-1285-45-532-311.
- [20] K. L. Williams, B. H. Phillips, P. A. Jones, S. A. Beaman, and P. J. Fleming, “Thermography in screening for breast cancer,” *Journal of Epidemiology and Community Health*, vol. 44, no. 2, pp. 112–113, 1990.
- [21] K. Maruyama, S. Mizushina, T. Sugiura, G. M. J. Van Leeuwen, J. W. Hand, G. Marrocco, F. Bardati, A. D. Edwards, D. Azzopardi, and D. Land, “Feasibility of noninvasive measurement of deep brain temperature in newborn infants by multifrequency microwave radiometry,” *Microwave Theory and Techniques, IEEE Transactions on*, vol. 48, no. 11, pp. 2141–2147, 2000.
- [22] J. W. Hand, G. M. J. V. Leeuwen, S. Mizushina, J. B. V. d. Kamer, K. Maruyama, T. Sugiura, D. V. Azzopardi, and A. D. Edwards, “Monitoring of deep brain temperature in infants using multi-frequency microwave radiometry and thermal modelling,” *Physics in Medicine and Biology*, vol. 46, no. 7, p. 1885, 2001.

- [23] T. Sugiura, Y. Kouno, A. Hashizume, H. Hirata, J. W. Hand, Y. Okita, and S. Mizushina, "Five-band microwave radiometer system for non-invasive measurement of brain temperature in new-born infants: system calibration and its feasibility," in *Engineering in Medicine and Biology Society, 2004. IEMBS '04. 26th Annual International Conference of the IEEE*, vol. 1, pp. 2292–2295.
- [24] J. K. Wyatt, A. R.-D. Cecco, C. A. Czeisler, and D.-J. Dijk, "Circadian temperature and melatonin rhythms, sleep, and neurobehavioral function in humans living on a 20-h day," *American Journal of Physiology - Regulatory, Integrative and Comparative Physiology*, vol. 277, no. 4, pp. R1152–R1163, 1999.
- [25] M. J. B. J. W. C. A. J. Y. C O'Brien, R W Hoyt, "Telemetry pill measurement of core temperature during active heating and cooling," *Medicine and Science in Sports and Exercise*, vol. 30, no. 3, pp. 468–472, 1997.
- [26] K. Stavem, H. Saxholm, and N. Smith-Erichsen, "Accuracy of infrared ear thermometry in adult patients," *Intensive Care Medicine*, vol. 23, no. 1, pp. 100–105, 1997.
- [27] R. H. Dicke, "The measurement of thermal radiation at microwave frequencies," *Review of Scientific Instruments*, vol. 17, no. 7, pp. 268–275, 1946.
- [28] C. Gabriel and et al., "The dielectric properties of biological tissues: I. literature survey," *Physics in Medicine and Biology*, vol. 41, no. 11, p. 2231, 1996.
- [29] H. P. Schwan, "Electrical properties of tissues and cell suspensions: mechanisms and models," in *Engineering in Medicine and Biology Society, 1994. Engineering Advances: New Opportunities for Biomedical Engineers. Proceedings of the 16th Annual International Conference of the IEEE*, pp. A70–A71 vol.1.

- [30] T. W. Athey, M. A. Stuchly, and S. S. Stuchly, "Measurement of radio frequency permittivity of biological tissues with an open-ended coaxial line: Part I," *Microwave Theory and Techniques, IEEE Transactions on*, vol. 30, no. 1, pp. 82–86, 1982.
- [31] K. S. Cole and R. H. Cole, "Dispersion and absorption in dielectrics i. alternating current characteristics," *The Journal of Chemical Physics*, vol. 9, no. 4, pp. 341–351, 1941.
- [32] K. S. Cole and R. H. Cole, "Dispersion and absorption in dielectrics ii. direct current characteristics," *The Journal of Chemical Physics*, vol. 10, no. 2, pp. 98–105, 1942.
- [33] H. Ljunggren, D. Ikkos, and R. Luft, "Studies on body composition," *Acta Endocrinologica*, vol. 25, no. 2, pp. 187–198, 1957, 10.1530/acta.0.0250187.
- [34] P. E. Watson, I. D. Watson, and R. D. Batt, "Total body water volumes for adult males and females estimated from simple anthropometric measurements," *The American Journal of Clinical Nutrition*, vol. 33, no. 1, pp. 27–39, 1980.
- [35] K. R. Segal, B. Gutin, E. Presta, J. Wang, and T. B. Van Itallie, "Estimation of human body composition by electrical impedance methods: a comparative study," *Journal of Applied Physiology*, vol. 58, no. 5, pp. 1565–1571, 1985.
- [36] M. Lazebnik and et al., "Ultrawideband temperature-dependent dielectric properties of animal liver tissue in the microwave frequency range," *Physics in Medicine and Biology*, vol. 51, no. 7, p. 1941, 2006.
- [37] S. W. Smye and et al., "Modelling the electrical properties of tissue as a porous medium," *Physics in Medicine and Biology*, vol. 52, no. 23, p. 7007, 2007.
- [38] S. Gabriel and et al., "The dielectric properties of biological tissues: II. measurements in the frequency range 10 Hz to 20 GHz," *Physics in Medicine and Biology*, vol. 41, no. 11, p. 2251, 1996.

- [39] S. Gabriel, R. W. Lau, and C. Gabriel, "The dielectric properties of biological tissues: III. parametric models for the dielectric spectrum of tissues," *Physics in Medicine and Biology*, vol. 41, no. 11, p. 2271, 1996.
- [40] H. Dieter, S. T. Staelin, J. Z. Tsai, S. Tungjitkusolmun, D. M. Mahvi, and J. G. Webster, "In vivo electrical conductivity of hepatic tumours," *Physiological Measurement*, vol. 24, no. 2, p. 251, 2003.
- [41] T. Yilmaz, T. Karacolak, and E. Topsakal, "Characterization and testing of a skin mimicking material for implantable antennas operating at ISM band (2.4 GHz-2.48 GHz)," *Antennas and Wireless Propagation Letters, IEEE*, vol. 7, pp. 418–420, 2008.
- [42] Y. Okano, K. Ito, I. Ida, and M. Takahashi, "The sar evaluation method by a combination of thermographic experiments and biological tissue-equivalent phantoms," *Microwave Theory and Techniques, IEEE Transactions on*, vol. 48, no. 11, pp. 2094–2103, 2000.
- [43] S. Jacobsen and P. R. Stauffer, "Multifrequency radiometric determination of temperature profiles in a lossy homogeneous phantom using a dual-mode antenna with integral water bolus," *Microwave Theory and Techniques, IEEE Transactions on*, vol. 50, no. 7, pp. 1737–1746, 2002.
- [44] S. Jacobsen and O. Klemetsen, "Improved detectability in medical microwave radiothermometers as obtained by active antennas," *Biomedical Engineering, IEEE Transactions on*, vol. 55, no. 12, pp. 2778–2785, 2008.
- [45] Z. Zhong Qing, L. Qing Huo, X. Chunjiang, E. Ward, G. Ybarra, and W. T. Joines, "Microwave breast imaging: 3-D forward scattering simulation," *Biomedical Engineering, IEEE Transactions on*, vol. 50, no. 10, pp. 1180–1189, 2003.

- [46] M. Lazebnik and et al., "Tissue-mimicking phantom materials for narrowband and ultrawideband microwave applications," *Physics in Medicine and Biology*, vol. 50, no. 18, p. 4245, 2005.
- [47] L. Hardell, K. H. Mild, A. Pahlson, and A. Hallquist, "Ionizing radiation, cellular telephones and the risk for brain tumours," *European Journal of Cancer Prevention*, vol. 10, no. 6, 2001.
- [48] R. A. Waldron, "Perturbation theory of resonant cavities," *Proceedings of the IEE - Part C: Monographs*, vol. 107, no. 12, pp. 272–274, 1960.
- [49] M. D. Janezic, E. F. Kuester, and J. Baker-Jarvis, "Broadband complex permittivity measurements of dielectric substrates using a split-cylinder resonator," in *Microwave Symposium Digest, 2004 IEEE MTT-S International*, vol. 3, pp. 1817–1820 Vol.3.
- [50] C. P. L. Rubinger and L. C. Costa, "Building a resonant cavity for the measurement of microwave dielectric permittivity of high loss materials," *Microwave and Optical Technology Letters*, vol. 49, no. 7, pp. 1687–1690, 2007.
- [51] J. Baker-Jarvis, M. D. Janezic, P. D. Domich, and R. G. Geyer, "Analysis of an open-ended coaxial probe with lift-off for nondestructive testing," *Instrumentation and Measurement, IEEE Transactions on*, vol. 43, no. 5, pp. 711–718, 1994.
- [52] X. Palomer, V. Topkar, and Z. Popovic, "Complex permittivity phantom tissue measurements using a TRL calibration fixture," *National Radio Science Meeting*, 2012.
- [53] M. Hiebel, "Vector network analyzer (VNA) calibration: The basics," 2008.
- [54] Agilent, "Agilent network analysis applying the 8510 TRL calibration for non-coaxial measurements. product note 8510-8a," 2000.
- [55] Agilent, "Hp: Free space materials measurements seminar," 2006.

- [56] A. M. Nicolson and G. F. Ross, "Measurement of the intrinsic properties of materials by time-domain techniques," *Instrumentation and Measurement, IEEE Transactions on*, vol. 19, no. 4, pp. 377–382, 1970.
- [57] W. B. Weir, "Automatic measurement of complex dielectric constant and permeability at microwave frequencies," *Proceedings of the IEEE*, vol. 62, no. 1, pp. 33–36, 1974.
- [58] G. F. Engen and C. A. Hoer, "Thru-Reflect-Line: An improved technique for calibrating the dual six-port automatic network analyzer," *Microwave Theory and Techniques, IEEE Transactions on*, vol. 27, no. 12, pp. 987–993, 1979.
- [59] D. Popovic, L. McCartney, C. Beasley, M. Lazebnik, M. Okoniewski, S. C. Hagness, and J. H. Booske, "Precision open-ended coaxial probes for in vivo and ex vivo dielectric spectroscopy of biological tissues at microwave frequencies," *Microwave Theory and Techniques, IEEE Transactions on*, vol. 53, no. 5, pp. 1713–1722, 2005.
- [60] X. Dong and Y.-H. Wang, "A broadband dielectric measurement technique: Theory, experimental verification, and application," *Journal of Environmental and Engineering Geophysics*, vol. 14, no. 1, pp. 25–38, 2009, 10.2113/JEEG14.1.25.
- [61] W. J. Ellison and J. M. Moreau, "Open-ended coaxial probe: Model limitations," *Instrumentation and Measurement, IEEE Transactions on*, vol. 57, no. 9, pp. 1984–1991, 2008.
- [62] Agilent, "Verification of on-wafer (SOLT) calibration," 2003.
- [63] A. Nyshadham, C. L. Sibbald, and S. S. Stuchly, "Permittivity measurements using open-ended sensors and reference liquid calibration-an uncertainty analysis," *Microwave Theory and Techniques, IEEE Transactions on*, vol. 40, no. 2, pp. 305–314, 1992.

- [64] S. Evans and S. C. Michelson, "Intercomparison of dielectric reference materials available for the calibration of an open-ended probe at different temperatures," *Measurement Science and Technology*, vol. 6, no. 12, p. 1721, 1995.
- [65] B. Bianco, A. Corana, L. Gogioso, S. Ridella, and M. Parodi, "Open-circuited coaxial lines as standards for microwave measurements," *Electronics Letters*, vol. 16, no. 10, pp. 373–374, 1980.
- [66] H. Levine and C. H. Papas, "Theory of the circular diffraction antenna," *Journal of Applied Physics*, vol. 22, no. 1, pp. 29–43, 1951.
- [67] A. A. Pistolkors, "Theory of the circular diffraction antenna," *Proceedings of the IRE*, vol. 36, no. 1, pp. 56–60, 1948.
- [68] V. A. F. A. L. Cullen and J. R. Wait, *Antennas in Inhomogeneous Media*, 1st ed., 1969.
- [69] M. Nives Parodi, C. Castagneto, G. Filaci, G. Murdaca, F. Puppo, F. Indiveri, and M. Scudeletti, "Plicometer skin test: a new technique for the evaluation of cutaneous involvement in systemic sclerosis," *Rheumatology*, vol. 36, no. 2, pp. 244–250, 1997, 10.1093/rheumatology/36.2.244.
- [70] P. Stark and D. Jaramillo, "CT of the sternum," *American Journal of Roentgenology*, vol. 147, no. 1, pp. 72–77, 1986.
- [71] IEEE, "Ieee standard for safety levels with respect to human exposure to radio frequency electromagnetic fields, 3 kHz to 300 GHz," *IEEE Std C95.1-1991*, p. 1, 1992.
- [72] H. O. Rolfsnes, P. F. Maccarini, S. Jacobsen, and P. R. Stauffer, "Design of spiral antennas for radiometric temperature measurement," in *Engineering in Medicine and Biology Society, 2004. IEMBS '04. 26th Annual International Conference of the IEEE*, vol. 1, pp. 2522–2525.

- [73] R. F. Schwartz, "Input impedance of a dipole or monopole," *Microwave Journal*, vol. 15, 1972.
- [74] C. A. Balanis, *Antenna Theory. Analysis and Design*. Wiley, 2005.
- [75] M. Kyungsik, H. Haewook, and P. Ikmo, "Terahertz folded half-wavelength dipole antenna for high output power," in *Microwave Photonics, 2005. MWP 2005. International Topical Meeting on*, pp. 301–304.
- [76] R. corporation, "RT/duroid 6006/6010LM high frequency laminates."
- [77] I. J. Bahl and S. S. Stuchly, "Analysis of a microstrip covered with a lossy dielectric," *Microwave Theory and Techniques, IEEE Transactions on*, vol. 28, no. 2, pp. 104–109, 1980.
- [78] L. Yang and N. Bowler, "Resonant frequency of a rectangular patch sensor covered with multilayered dielectric structures," *Antennas and Propagation, IEEE Transactions on*, vol. 58, no. 6, pp. 1883–1889, 2010.
- [79] L. Yang, N. Bowler, and D. B. Johnson, "A resonant microwave patch sensor for detection of layer thickness or permittivity variations in multilayered dielectric structures," *Sensors Journal, IEEE*, vol. 11, no. 1, pp. 5–15, 2011.
- [80] V. Sekar, W. J. Torke, S. Palermo, and K. Entesari, "A self-sustained microwave system for dielectric-constant measurement of lossy organic liquids," *Microwave Theory and Techniques, IEEE Transactions on*, vol. 60, no. 5, pp. 1444–1455, 2012.
- [81] E. R. Adair, *Microwaves and Thermoregulation*, 1983.